Progress in Materials Science 142 (2024) 101225

Contents lists available at ScienceDirect

Progress in Materials Science

journal homepage: www.elsevier.com/locate/pmatsci

Simulation methods for self-assembling nanoparticles

Petr Král [a,b,c], Henry Chan [d], Lela Vuković [e], Sanoj Raj [a], Soumyo Sen [a], Yanxiao Han [a], Michal Sawczyk [a]

[a] Department of Chemistry, University of Illinois at Chicago, Chicago, IL, USA
[b] Department of Physics, University of Illinois at Chicago, Chicago, IL, USA
[c] Department of Pharmaceutical Sciences, University of Illinois at Chicago, Chicago, IL, USA
[d] Center for Nanoscale Materials, Argonne National Laboratory, Argonne, IL, USA
[e] Department of Chemistry and Biochemistry, University of Texas at El Paso, El Paso, TX, USA

A B S T R A C T

In the last decades, nanoparticles (NPs) have been assembled into clusters, low-dimensional superstructures, crystallites, and bulk materials. Typically, the self-assembly processes are controlled by competing and relatively complex interactions acting between the nanoscale components, which depend on the types of NPs, solvents, and external fields. Here, we show how selected mean-field, coarse-grained, atomistic, and quantum simulation methods are used at different scales to describe systems of self-assembling NPs studied experimentally. These simulation methods can provide in-depth understanding of the processes active during the formation of these systems.

1. Introduction

Molecular self-assembly and disassembly at many spatial and time scales play a central role in biology [1]. Accordingly, the self-assembly of synthetic material components with a large variety of characteristics and terminal structures has been investigated [2–4]. Gradually, colloidal nanoparticles (NPs) of different material compositions, sizes, shapes, and ligands have been synthesized and self-assembled in different solvents, system conditions, and external fields into myriads of clusters, superstructures, and lattices [5–9]. Typically, the colloidal NPs self-assemble in bulk solutions [10], on solid substrates [11], or at liquid–air interfaces [12–14], and eventually become dried.

The NP-self-assembly processes are guided by a delicate interplay of various forces of comparable magnitudes acting between the system components [15,16]. These forces originate in van der Waals (vdW) [17], electrostatic [18], hydrophobic [19], magnetic [13], hydrogen-bonding mediated [20], and other interactions [31], associated with the types of NP-core materials, ligands, solvents, and self-assembly conditions used. Once the solvent is removed, the free energies of binding between NPs becomes dramatically increased and the structures become stabilized.

To design NP-based coarse materials with specific properties, the NP-self-assembly processes must be well understood. In order to disclose the nature of forces stabilizing selected self-assembled structures, the parameters of these systems need to be well known and the systems should be modeled accordingly [21–23]. Historically, the NP self-assembly was studied semi-analytically [24,25] or by simulations performed at mean-field [26–28], coarse-grained [29], and atomistic levels [30]. In principle, each of these approaches provides a different precision of description and it works best at certain spatial and time scales that should be fitted to the information sought.

The approximations used in the simulations can be selected by considering how well the experimental system is known, the necessary system size and length of simulations, and the expected modeling precision. It is always necessary to use a common sense

E-mail address: pkral@uic.edu (P. Král).

https://doi.org/10.1016/j.pmatsci.2023.101225
Received 19 March 2023; Received in revised form 11 November 2023; Accepted 4 December 2023
Available online 8 December 2023
0079-6425/Published by Elsevier Ltd.

based on good intuition. Mean-field methods can often provide a qualitative or even semi-quantitative agreement between the experimental and modeling results in systems of self-assembling nanoscale components. However, finding a precise quantitative agreement with these experiments can be very challenging since the exact conditions of such experiments are not fully known, including the exact nature of the involved components. When knowledge of the system is satisfactory, atomistic simulations can be used to provide highly reliable modeling results. However, quantum calculations need to be used to provide atomistic parameters of the systems. Also, some interactions might need to be added in the simulations, such as long-range van der Waals interactions between solid components. To better understand these interactions, *in situ* TEM studies of NPs self-assembly in liquid cells have been performed and correlated with precise simulations [20,32].

Here, we show how one can model the self-assembly of NPs with a relatively complex coupling using modeling techniques of different precision. First, we show how the self-assembly processes and structures formed can be modeled when NPs have a short-range vdW and long-range electric or magnetic coupling, described by mean-field semi-analytical and Monte Carlo techniques. Second, we show how the self-assembly of larger NP-molecular systems can be described by coarse-grained molecular dynamics (MD) simulations. Third, we show how relatively precise atomistic MD simulations can be used when NPs with complex ligands are coupled in realistic solvents, where some interactions might be modeled by quantum methods. Finally, we present atomistic MD simulations of selected *in situ* NPs self-assembly experiments to reveal microscopic dynamical processes active during the formation of these systems. In these

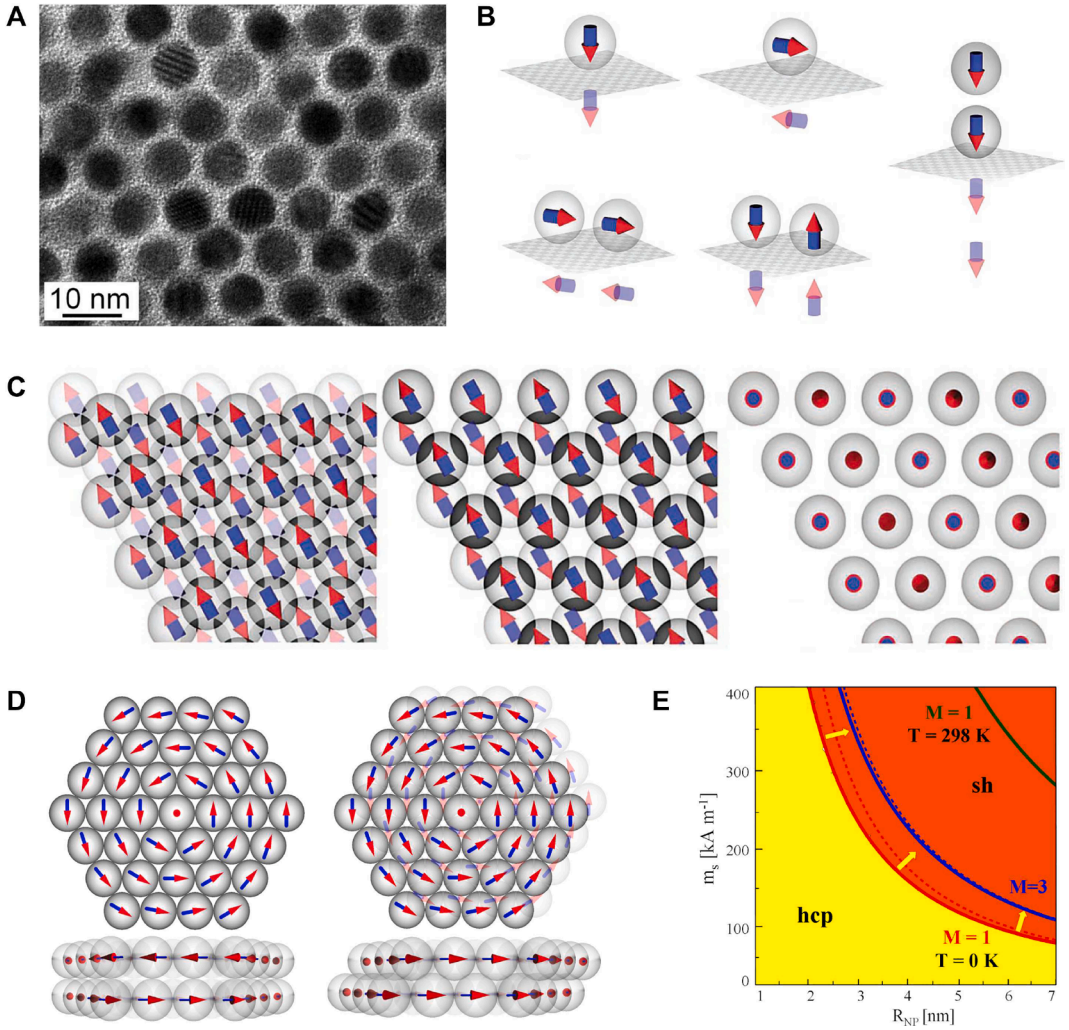

Fig. 1. (A) Transmission electron microscopy (TEM) image of a superlattice of 7.2 nm PbSe NPs, where the space around each NPs is clear of other NPs, pointing to the simple hexagonal (sh) stacking (Moiré fringes seen) [33]. (B) Typical configurations of NPs on graphite, where image charge Coulomb coupling of NPs with the substrate takes part. (C) Dipole ordering in NPs superlattices. Top view ([0001] plane) of horizontal antiferroelectric ordering in fcc (left), horizontal antiferroelectric ordering in hcp (middle), and vertical antiferroelectric ordering in sh lattices (right). (D) Stable configurations of magnetic NPs with dipolar coupling in two parallel plaques (left - sh, rigth - hcp). (E) The phase diagram for such NPs with a bulk vdW coupling plotted as a function of the NP-radius, R_{NP}, and the saturation magnetization, m_s (M - the number of NPs circumferences in the plaquets). At $T = 298$ K, the phase boundary shifts. [35].

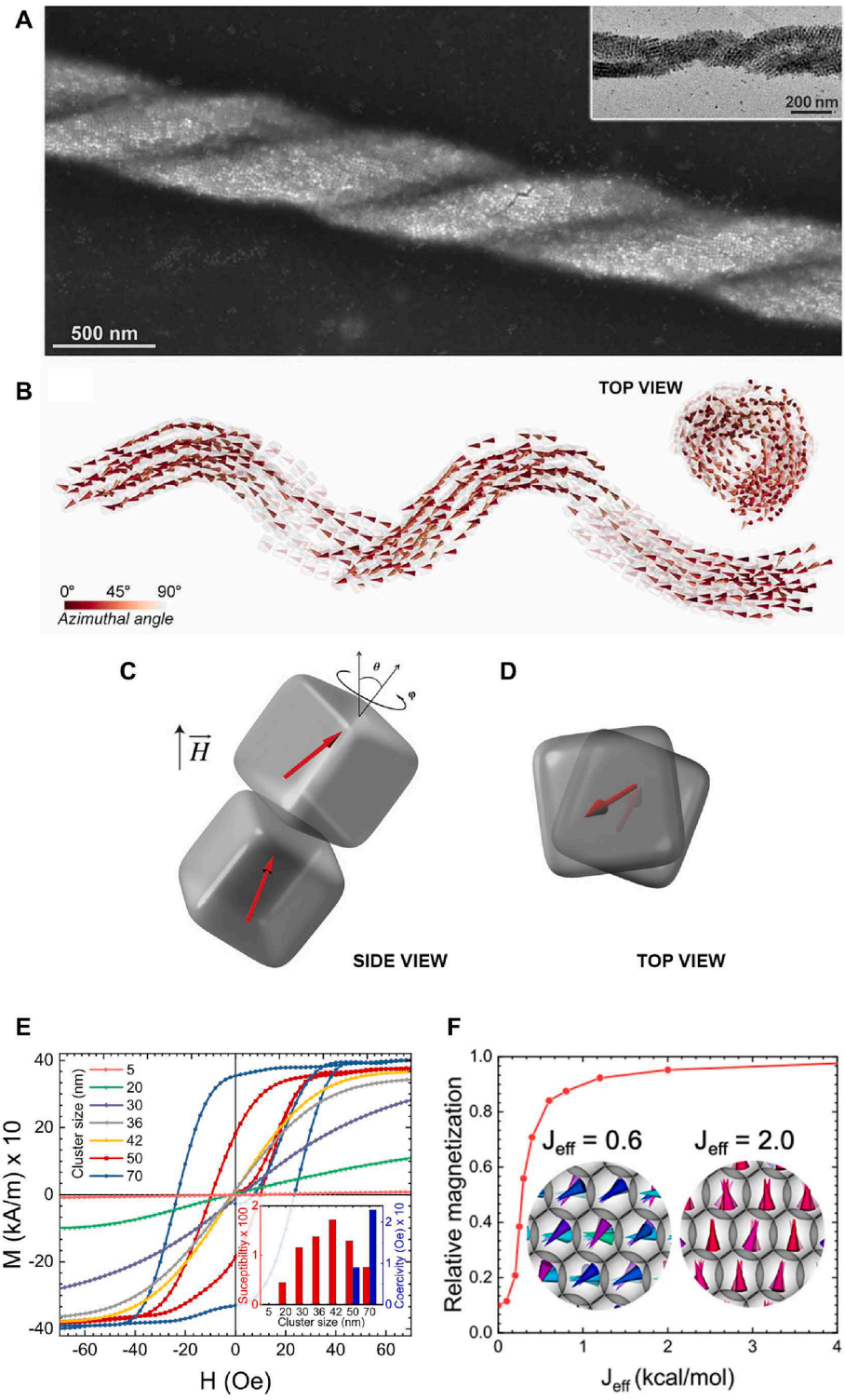

Fig. 2. (A) Scanning electron microscopy (SEM) image of a well-defined double helix. (inset) TEM image of two belts wrapping around each another. (B) Snapshots from Monte Carlo simulations of a one-dimensional belt folding into a helix. (C) Typical configuration of two cubes in an external field, $H = 167$ G (vertical z-orientation) at $T = 300$ K (bulk vdW coupling is reduced by $1/2$ with respect to the nominal value). (D) View along the cube axis reveals that the nanocube pair is (transiently) chiral. Magnetic dipoles are represented by arrows. (bottom) Averaged orientation of dipoles in a thick filament under relatively weak external field ($H = 167$ G). The top two layers are purposely separated from the structure (left) to better illustrate the dipole arrangement. (E) The magnetization of SPM-clusters of different sizes. (inset) The susceptibility and coercivity of these clusters. (F) Relative magnetization of the cluster at different J_{eff}. (inset) NPs spin arrangement at $J_{eff} = 0.6$ and 1.2 kcal/mol.

examples, we identify and evaluate the dominant coupling interactions acting between the self-assembling nanoparticles, describe the formation of a rich types of NP-superstructures, and analyze their stability.

2. Mean-field modeling of self-assembling nanoparticles

In order to obtain the first insight into the conditions that control the self-assembly of NPs, one can often model these systems by DLVO and related mean-field methods that can be relatively easily implemented in large systems of many particles [26]. Despite the fact that systems are not simulated with these methods in atomistic details, the mean-field interparticle forces can be derived for NPs with bulk and surface Coulombic, van der Waals (bulk), hydrophobic (surfaces), and other couplings. Such mean-field semi-analytical modeling can be extended to self-assembling NPs coupled with a long-range electric or magnetic dipole–dipole coupling [33–35]. If the mean-field parametrization is carefully performed, the level of precision can be often satisfactory, giving at least a qualitative agreement. Unfortunatelly, various effects associated with atomistic details, such as the ligand entropy, are clearly missing in mean-field approaches.

2.1. Superlattices with dominant dipole–dipole coupling

In many early self-assembly experiments, relatively simple NPs were studied. For example, nearly spherical CdSe, PbSe and PbS NPs coated by oleic acid were placed in tetrachloroethylene above a carbon-coated substrate [33]. Upon evaporation of the solvent, it was found that these NPs with small diameters formed closed packed fcc and hcp superlattices, but NPs with larger diameters (above 7 nm) often self-assembled into hexagonally ordered vertical columns, producing a simple hexagonal (sh) structure (space group P6/mmm), as shown in Fig. 1 A. Nonlocal electric dipolar moments of NPs, arising due to the crystal structure type, asymmetric truncations of the crystal, and other reasons, were assumed to be responsible for the formation of these superlattices with a loose packing.

In the semi-analytical modeling, Coulombic coupling between individual nanoparticles was modeled by non-local electric dipoles, where two opposite point charges were symmetrically placed on the opposite sides (surfaces) of each NP. The interactions between the point charges q_m and q_n of different NPs were described by the Coulombic coupling,

$$V_{mn}\left(r_{mn}\right) = \frac{q_m q_n}{4\pi\epsilon r_{mn}}, \tag{1}$$

where ϵ is the dielectric constant and r_{mn} is the distance between these charges placed on different NPs. In a similar manner, the coupling between NPs and their images in conducting surfaces have been evaluated; note that dipole–dipole interactions between well separated (local) dipoles are attractive when two parallel dipoles are (above each other) within a cone with an azimuthal angle of $\theta < \cos^{-1}(1/\sqrt{3}) \approx 54^{\circ}$. Finally, the (bulk) vdW coupling between spherical NPs was described using the Hamaker formula [36]

$$W_{ij}^{vdW} = -\frac{A}{12}\left\{\frac{R}{d_{ij}\left(1+\frac{d_{ij}}{4R}\right)} + \frac{1}{1+\frac{d_{ij}}{R}+\frac{d_{ij}^2}{4R^2}} + 2\ln\left(\frac{d_{ij}\left(1+\frac{d_{ij}}{4R}\right)}{R\left(1+\frac{d_{ij}}{R}+\frac{d_{ij}^2}{4R^2}\right)}\right)\right\}. \tag{2}$$

Here, R is the particle radius, d_{ij} is the distance between the surfaces of ith and jth nanoparticles, and A is the Hamaker constant evaluated for a given combination of the NPs body material and solvent used.

The energetics of NP clusters and lattices presented in Fig. 1 B, C revealed that NPs with non-local (electrical) dipolar coupling can form vertical stacks on conducting substrates, with antiparallel arrangements of dipoles in neighboring stacks. Similar observations were made for nanorods with dipolar moments [34]. Modeling studies have revealed that NPs with a dominant dipolar coupling can form superstructures with many types of dipolar ordering [35]. In particular, the sh ordering can be formed in hexagonal plaquets, when dipolar moments in neighboring plaquets run in opposite circular directions (Fig. 1 D). When the bulk vdW coupling between NPs is included in these plaquets, a phase diagram with sh and hcp regions can be obtained, as shown in Fig. 1 E [35].

2.2. Cooperative self-assembly of superparamagnetic nanocubes

When NPs interact by long-range interactions, many of them need to be simultaneously modeled to describe their cooperative behavior taking part during their self-assembly. The self-assembly of superparamagnetic (SPM) nanocubes (NCs) is a great example of systems for which mean-field methods were developed and implemented [13]. In the experiments, Fe_3O_4 NCs (average edge length = 13.4 nm) were covered by oleic acid (OA), solvated in evaporating hexane (excess of OA) and self-assembled at a diethylene glycol (DEG) surface (non-solvent) in magnetic fields of $H = 0 - 700$ G. The superstructures formed depended on the NCs coverage of a DEG surface. At lower coverages, $\chi < 1.5$, various linear superstructures formed with one or more layers of NCs. However, the most interesting parallel helices, seen in Fig. 2 A, formed at relatively high NCs coverages of $\chi > 1.5$.

In order to understand the formation of these large systems of many NCs stabilized by colloidal (non-magnetic) and magnetic interactions, hybrid mean-field Monte Carlo (MC) codes have been developed [13,37], where the self-assembly dynamics associated with all degrees of freedom of NCs were simulated simultaneously. At room temperature, each small magnetite SPM NC possessed a super-dipole (single magnetic domain) whose orientation was thermally fluctuating. Above a certain NC size or at low temperatures,

the NC super-dipole is in a blocked state, due to the magnetocrystalline anisotropy (MA) barrier; in larger real NCs (50 −70 nm), magnetic domains could also form. In the simulations, the super-dipole of a single magnetic domain was represented by a point dipole located in the center of each NC.

The simulated super-dipoles were partially aligned by a Zeeman coupling with an external magnetic field, and their motion was restrained with respect to the NC-axes by MA [13]. Therefore, the super-dipole (index i) had the Zeeman and MA energies, $E_i = E_i^Z + E_i^A$. Here,

$$E_i^Z = -K_Z\left(\vec{H}\cdot\vec{M_i}\right), \tag{3}$$

where $\vec{H}$ is the vector of an external magnetic field, and $\vec{M_i}$ is the magnetic dipole unit vector of the chosen NC. By limiting to the quartic term in bulk magnetite (Fe_3O_4), the MA energy is given by,

$$E_i^A = K_{A1}\left[\left(M_{ix}^{'}M_{iy}^{'}\right)^2 + \left(M_{ix}^{'}M_{iz}^{'}\right)^2 + \left(M_{iy}^{'}M_{iz}^{'}\right)^2\right], \tag{4}$$

where $M_{ix}^{'}, M_{iy}^{'}, M_{iz}^{'}$ are the components of the magnetic dipole unit vector in the NC coordinates. The quartic term generates "easy" and "hard" magnetization axes of the NCs, which are oriented along the cube body diagonals and edges, respectively. The dipole–dipole coupling energy of two super-dipoles within different NCs is

$$E_{ij}^{dd} = K_d\left(\frac{\vec{M}_i\cdot\vec{M}_j}{\left|\vec{r}_{ij}\right|^3} - \frac{3\left(\vec{M}_i\cdot\vec{r}_{ij}\right)\left(\vec{M}_j\cdot\vec{r}_{ij}\right)}{\left|\vec{r}_{ij}\right|^5}\right). \tag{5}$$

Here, K_d is the intrinsic magnetic moment of a homogeneously magnetized NC, and $\vec{r}_{ij}$ is a vector connecting the centers of both NCs. Surface coupling of NCs (ligands, solvent) was also approximately described by the MC code [13], but a bulk vdW coupling of NCs pairs was neglected for simplicity.

During MC simulations, a NC–helix was observed to form in Fig. 2 B from a straight pillar of pre-assembled NCs. The helicity was caused by a *spontaneous symmetry breaking* that originated from preference of NCs pairs to be slightly misaligned, due to frustrated symmetries of different interactions between them [37], as shown in Figs. 2 C, D. The vdW coupling leads to the preference of NCs to be in a facet-to-facet arrangement. However, this is not the lowest energy of coupled super-dipoles which are aligned in both NCs along their body diagonals. When the two NCs are slightly misaligned, their total energy can be lowered, giving rise to the helix formation.

Recently, these MC simulations were extended to describe extraordinary magnetic properties observed in clusters of Fe_3O_4 (≈ 5 nm) SPM NPs, which were partly regrown to have a medium exchange coupling. To model the exchange interaction between the NP-superspins, we have added in the above model the term,

$$E_{AB}^{exch} = -J_{atomic}\sum_{ij}\mathbf{s}_i\cdot\mathbf{s}_j \approx -J_{eff}\,\mathbf{S}_A\cdot\mathbf{S}_B. \tag{6}$$

Here, the atomic spins $\mathbf{s}_{i,j}$ coupled in the area of overlapping (A, B) NPs by the atomic exchange constant J_{atomic} were replaced by NP-superspins $\mathbf{S}_{A,B}$ coupled with an effective exchange constant J_{eff}. It turned out that a moderate $J_{eff} = 0.6$ kcal/mol can provide significant coupling between the superspins for them to form a much larger *global superspin* of the cluster. Yet this NP-coupling is loose enough to allow each NP to overcome the magnetic anisotropy barrier somewhat on its own. This causes a dramatic increase in the magnetic susceptibility of these NP-clusters which remain in SPM states up to much larger cluster sizes than solid particles. Fig. 2 E reveals the magnetization behavior of these NP-clusters of different sizes and their transition from SPM to blocked states, which is completely analogous to such behavior observed in clusters of a fixed size but increasing J_{eff}. Fig. 2 F also describes the relative magnetization of the global superspin of the NP-cluster in dependence on J_{eff}, showing that the superspins become practically aligned at $J_{eff} = 1-2$ kcal/mol.

3. Coarse-grained molecular dynamics simulations of NP-molecules co-assembly

Mean-field methods might have insufficient precision when colloidal NPs interact predominantly through their complex ligands. To better capture such molecular interactions, one could use coarse-grained molecular dynamics (CGMD) simulations, where groups of atoms or molecules can be approximately represented by different types of beads, partly preserving the molecular chemistry. However, given the approximate description of the ligands and solvents, one can again expect a qualitative agreement with the experiments. For more complex ligands, the precision might be inadequate. For example, this approach is lacking entropic and selective enthalpic contributions of individual atomic groups. Nevertheless, the reduced number of degrees of freedom (with respect to atomistic systems) allows CGMD simulations to run relatively fast, so that large or dynamical systems could be modeled.

Here, several self-assembling nanoparticle systems studied by CGMD simulations are briefly presented as an illustration of the approach. First, we present CG Au NPs with a core diameter of $d \approx 1.6$ nm, capped with dodecanethiol ligands, that were parametrized by the Martini 2.0 force-field [38]. On the water surface, these NPs can form stable membranes of good mechanical properties. The NPs can also be arranged to form free standing capsules, which can carry a molecular cargo, as shown in Fig. 3 (A).

Next, Fig. 3 B shows CGMD simulations of graphene intercalated inside a biological membrane formed by 1-palmitoyl-2-oleoyl-snglycero-3-phosphocholine phospholipids (POPC) [39]. Graphene sheets present in biological membranes can affect their activities or be cytotoxic. Fig. 3 C shows that graphene can also fold in various superstructures, enclosing liquids in cell-like environments [40,41] (atomistic MD simulations).

Finally, Fig. 3 D shows CGMD simulations of hydrated POPC liposomes with Au nanodisks (NDs) intercalated in its double-walls [42]. Partial equilibration of this hybrid ND-liposome for ≈ 150 ns provides stabilized superstructures, where the intercalated NDs preserve the lipid vesicle. Fig. 3 E shows a standalone nanopore formed between 6 NDs intercalated within a flat POPC bilayer, which was CGMD-simulated for 200 ns. Water chains can be observed to form in nanopores (channels) emerging between the tips of NDs. In general, the penetration of nanoparticles into biological membranes can be a complex cooperative process. The stabilization of membranes and nanoparticles within them has a slow and intriguing dynamics, which was modeled by different techniques [43–45].

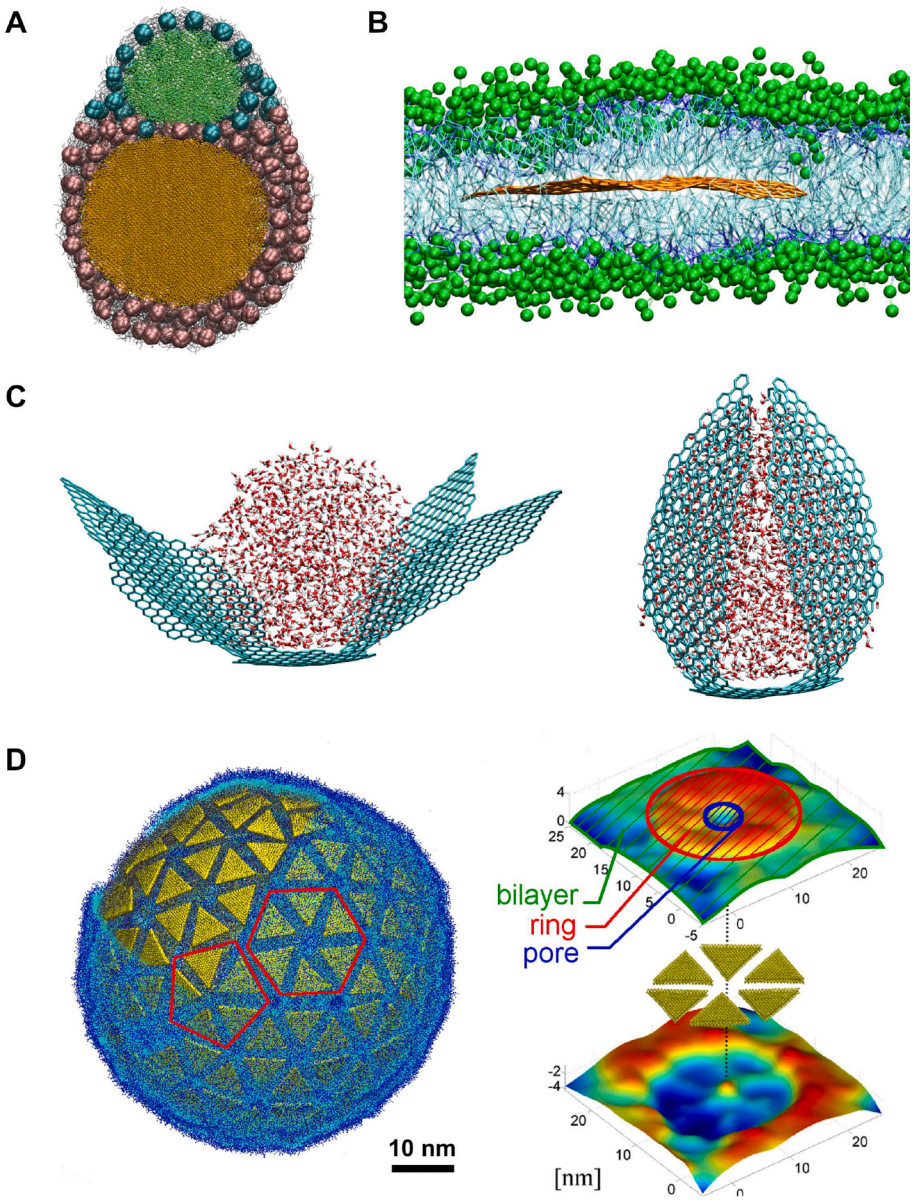

Fig. 3. (A) Sectional view of two water filled containers formed by Au NPs with alkanethiol ligands. (B) Graphene sheet hosted inside a POPC phospholipid bilayer membrane. (C) Co-assembly of graphene flake on a water droplet (atomistic MD). (D) Stabilization of nanodisks within spherical and planar POPC bilayers. (left) Hybrid NP-liposome ($d \approx 30$ nm) with 180 intercalated triangular NDs solvated in water after 150 ns equilibration. A portion of the lipids at the top are hidden to better show the NDs organization. Representative 5 (pentagon) and 6 (hexagon) ND clusters are marked. (right) A cluster of such 6 triangular NDs inside a POPC bilayer, equilibrated for 200 ns. A color map surface is fitted to the polar heads of the lipid molecules to show the bilayer structure.

4. Atomistic modeling of NPs self-assembled into clusters, low-D superstructures, crystallites, and lattices

In many current experiments, complex, competitive, cooperative, and fuel-driven interactions acting between colloidal ligated NPs can guide the formation (kinetics) of various superstructures and provide their stabilization (thermodynamics). Given the non-equilibrium nature of these complex self-assembly processes, the NP-structures formed can end up in metastable (kinetically trapped) states. To reliably predict the type of structures formed, we need to precisely describe the dominant interactions acting between the system components and cautiously analyze their possible contributions to the self-assembly processes. In principle, most of these interactions can be precisely captured by well-parametrized classical force-fields obtained through first principle (*ab initio*) quantum calculations performed at conditions (solvents) that are as close as possible to the actual experiments [46]. When such force-fields are used in atomistic MD simulations, the obtained results could quantitatively agree with the experiments, as discussed in the follow up examples.

In the presented MD simulations, the atomistic structures of NPs and solvents were prepared with various means, such as GaussView (molecules), VMD [47], and customized codes (NPs). The parameters of these components were described with a CHARMM force-field (non-reactive), expanded for new molecules by standard procedures [48]. Atomistic MD simulations of the systems were carried with NAMD [49]. Typically, the systems were simulated by the Langevin dynamics in boxes filled with solvents held at normal conditions (NPT or NVT ensembles), with periodic boundary conditions applied to capture a long-range Coulombic coupling [50].

4.1. Self-standing porous NP-membranes

Initially, atomistic MD simulations were used to study the structure, stability, and various activities of relatively simple NP-assemblies [51,52]. For example, they were used in the modeling of dodecanethiol-coated Au NPs ($d \approx 5$ nm diameters) that were experimentally shown to self-assemble into 2D membranes on a water surface (Fig. 4 A). These self-standing NP-membranes can be removed from water, be stacked on the top of each other (4 layers), and used in molecular filtration. Moreover, it was shown that biomolecules with diameters of $d_M < 1-1.2$ nm can easily pass through the NPs membranes, while larger molecules cannot pass through [51].

To understand the membrane transport mechanisms present in these experimental studies, NP-membranes with a perfect close-packed hexagonal arrangement of identical NPs were stabilized in MD simulations at the water–air interface (Fig. 4 B). However, the Gibbs free energies calculated for molecules passing along the pathway between 3 neighboring NPs revealed a large barrier even for small molecules like water, due to high NP-ligand densities, preventing the molecules from passing the NP-membrane (steric effects) [51]. When a small disorder in NP-sizes and ligand densities was introduced in the membrane, in accordance with the experimental observations, the membrane has developed nanopores of sizes roughly matching the molecules observed to pass the experimental membranes (Fig. 4 C). These atomistic MD simulations determined that a size-exclusion mechanism is responsible for the molecular filtration observed in these NP-membranes.

4.2. Cooperative self-assembly of chiral NPs into helical ribbons

Colloidal nanoparticles with more complex shapes and ligands can self-assemble into many other structures. For example, when a racemate of chiral CdTe NPs was irradiated by a circularly polarized light, decomposition of thioglycolic acid stabilizers and Te → S exchange underwent in one enantiomer of NPs, which became transformed into "bare" CdS NPs (5–6 nm) [24]. These light-preselected left or right CdS NPs self-assembled into left- or right-handed ribbons (Figs. 5 F, G), respectively.

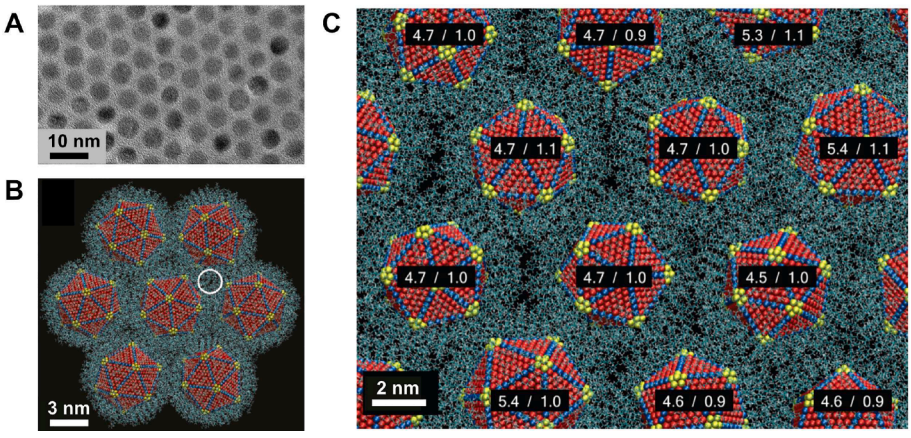

Fig. 4. (A) Transmission electron microscopy (TEM) image of monolayer of dodecanethiol-coated gold nanocrystals. (B) Snapshot from an atomistic simulation of the nanocrystal layer with perfectly identical NPs. (C) In the presence of disorder in the NPs sizes and densities of ligands, nanopores emerge between the NPs. The diameter d (in nm) and the ligand density χ are indicated on each nanocrystal as d/χ.

These NPs were MD simulated atomistically as 3.6 nm tetrahedra cut from a cubic CdS crystal, which were asymmetrically truncated at their vertices to be chiral (Figs. 5 A-C). The simulated NPs were kept "bare", but the large polarity of the CdS lattice, calculated by *ab initio* methods in vacuum, was reduced at the NP surfaces to account for possible residual ligands and the reduction (depolarization) of CdS local charges in water. Each NP was assigned a total charge of $-2e$ (homogeneously spread on the NP atoms), roughly fitting the experiments. A bulk vdW coupling between the NP-cores was added to the force-field, which had ($\approx$ 1 nm) cut-off implemented on the atomistic vdW coupling.

The left-handed and right-handed NPs were separately pre-assembled into flat ribbons and simulated in water with Cl^- counterions. In these solvated ribbons, NPs were attracted by their bulk vdW coupling, Coulombic coupling between their polar edges, and their partial hydrophobicity, while their Coulombic repulsion caused by charging was screened by counterions. Water molecules were observed to form a soft "cushion" layer between neighboring NPs, allowing them to slightly translate and reorient with respect to each other. The simulated ribbons gradually twisted in opposite directions, as shown in Figs. 5 D, E, in analogy to the experimental systems, seen in Figs. 5 F, G. The ribbon twists originated in the NPs chirality (truncations), which was *cooperatively* promoted via solvent-assisted NP-NP coupling.

4.3. pH-dependent self-assembly of sticky NPs into hollow capsules

In related experiments, charged tetrahedral CdS NPs without extraneous molecular coating were observed to self-assemble into hollow capsules in solutions with moderately basic pH and ionic strength of 0.8 mM [18], as shown in Fig. 6 A. A cryo-TEM tomography (Fig. 6 B) confirmed that these porous nanoshells had pH-dependent sizes of 10 $-$25 nm diameters and wall thickness of

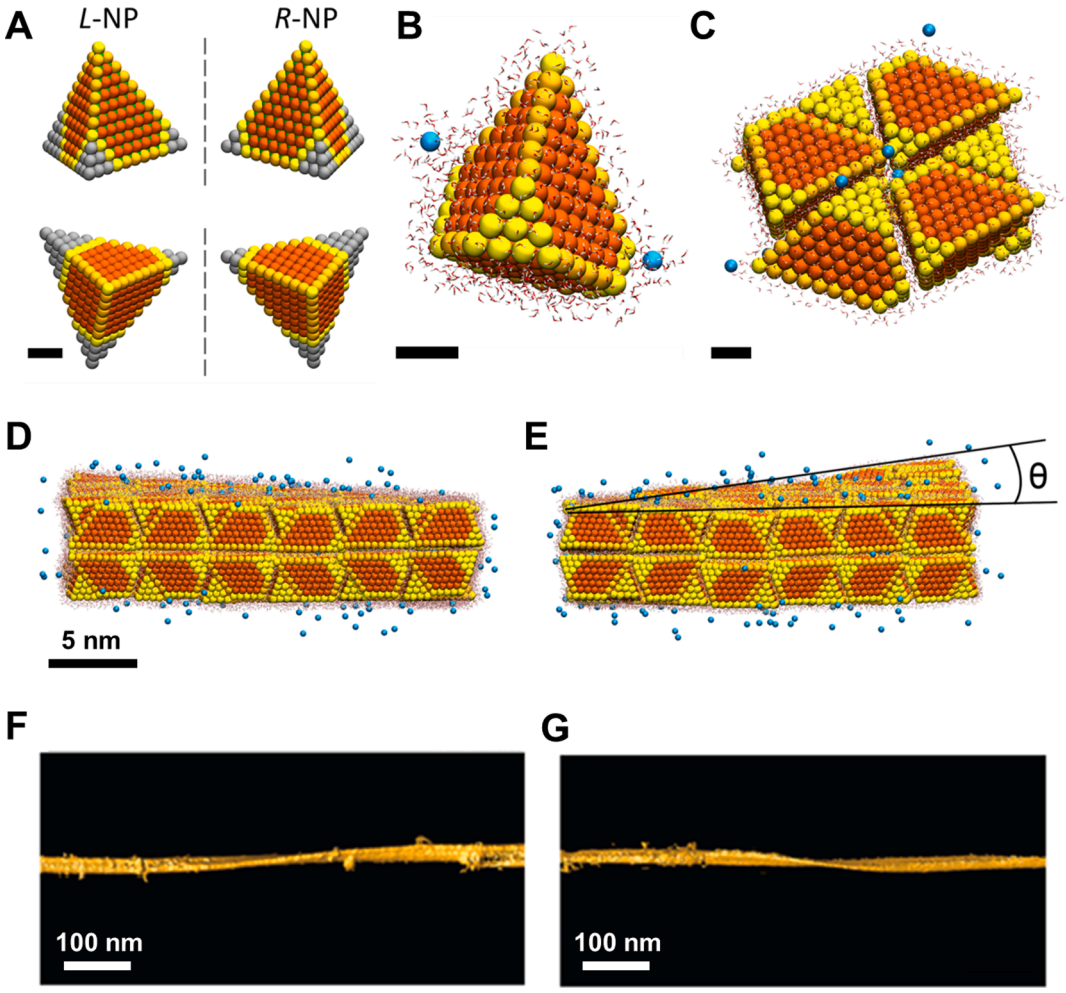

Fig. 5. MD simulations and experimental studies of self-assembly of chiral NPs. (A) Atomistic models of NPs with left-handed (LH) and right-handed (RH) truncations used in MD simulations. (B) Detailed view of a single NP in aqueous environment with counter ions used in MD simulations. (C) A fragment of the simulated self-assembled ribbon (top view) displaying packing of NPs. Scale bars in (A-C) are 1 nm. (D) and (E) Side views of simulated NP ribbon with LH (D) and RH (E) truncated NPs. Dihedral angle θ determines the pitch of the nanoribbons. (F) and (G) Surface rendering of 3D TEM tomographic reconstruction of LH (F) and RH nanoribbon (G).

3 −5 nm (NP size), accommodating up to 90 NPs. At pH = 5, only solid clusters with ≈ 20 NPs were formed. However, at pH = 7.2,8.2, and 9.5, hollow capsids with diameters of 11, 16, and 22 nm were formed, respectively [18]. The ζ potentials and cavity charges measured in the last three cases gave NP average charges of $q \approx 0.3$ e, 0.6 e, and 0.9 e. When the ionic strength was increased from 0.8 mM to 5.8 mM, the Coulombic repulsion between the charged NPs was dramatically shortened, so that only solid NPs clusters were formed.

The formation of pH-dependent NP-shells, as well as the shell-size and wall-thickness uniformity indicated a possible self-limiting (total cluster charge-controlled) growth, analogous to that observed in cavity-less NP clusters [53]. However, the hollow nature of capsules pointed to their more complex stabilization. Since the cavities inevitably formed as a result of repulsive Coulombic forces between the charged NPs, relatively strong local attractive (locking) forces inevitably prevented the separation of NPs.

Initially performed mean-field DLVO modeling, based on a simple balance of bulk vdW and mean electrostatic forces acting between charged NPs [18], didn't reproduce the experimental observations. Therefore, we performed realistic atomistic MD simulations of capsids formed by truncated tetrahedra CdS NPs (2.4 nm). The NPs were randomly covered by simple chemical groups typical for aqueous media, e.g., OH^-, H_2O, and H^+, corresponding to basic, neutral, and slightly acidic aqueous media (Fig. 6 C), which emphasized the effect of local hydrogen bonding. MP2-level *ab initio* calculations of small CdS crystallites with these groups were performed in water [18]. Beside these atomistic charges, the total charges of NPs were chosen to match the zeta-potential measurements. The vdW coupling between the NP cores was separately added to the force field.

Fig. 6 D shows one of such capsules stabilized in water, which contain sodium cations to neutralize the charged NPs. These MD simulations fitted well the experimental observations and revealed that the NP-locking mechanism was established by residual groups present at the NPs surfaces, forming multiple hydrogen and other physical bonds between neighboring NPs being in a direct contact with each other (multivalent binding) [46]. In principle, such systems can be in metastable or fully non-equilibrium conditions [54]. Additional studies of such complex systems with ionic solutions can be also performed by machine learning codes [55].

4.4. Self-assembly of NPs with a tunable coupling between ligands

The material, shape, and size of NPs, the structure, length, and density of ligands, and other factors can affect the chemistry of groups that are most exposed to the solvent [46,56–58]. In turn, these groups affect the solubility of NPs, which can be used to control

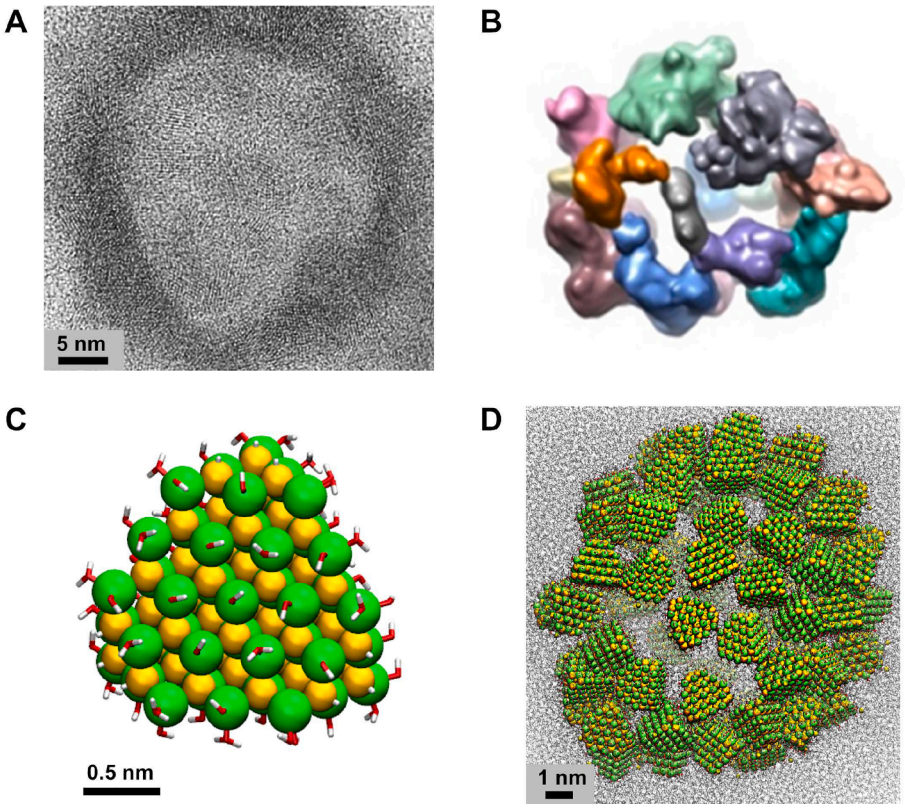

Fig. 6. (A) TEM image of a CdS nanoshell (≈ 25 nm) obtained at pH = 9.5. (B) 3D image of a nanoshell obtained by TEM tomography at 77 K, with differently colored NP domains separated by nanopores. (C) Structural representation of NPs carrying H_2O, OH^-, and H^+ surface ligands typical for neutral and slightly acidic media (S - yellow, Cd - green spheres in the NP core, O - red, and H - white). (D) Snapshot of pre-assembled NPs that carry $q = 0.9$ e after 22 ns of equilibration.

their self-assembly.

Fig. 7 shows NPs covered by amphiphilic moieties with terminal residues of $R_1=(CH_2)_5CH_3$ and $R_2=(CH_2)_{15}CH_3$, which were atomistically simulated in water and methanol (hydrophobic). This example shows that the hydrophobicity of ligated NPs depends on the chemistry of ligands and their overall organization, which in turn can strongly depend on the solvent type. Fig. 7 reveals that the terminal hydrophobic alkyl moieties are largely hidden in water, but they are extended outwards in methanol, thereby increasing the NP-hydrophobicity. This exposure can be quantified by calculating the solvent accessible surface area (SASA) of different chemical groups in the ligands. Here, SASA for all C in the terminal residues R_1 resp. R_2 are 1.5 resp. 2.1 times larger in methanol than in water. Therefore, the longer R_2 residues can be more adjusted to the solvent and thus affect the NPs solubility and self-assembly.

Recent studies have revealed that the chemistry of NP-ligands could be also controlled by external stimuli, such as light [59]. In these experiments, small Au NPs functionalized by azobenzene ligands were solvated in toluene. When the system was exposed to light of different wavelengths, the azobenzene ligands switched between trans and cis isomers, as shown in Fig. 8 A, and NPs have reversibly assembled (cis form) or dis-assembled (trans form). In the cis azobenzene, two dipoles of nitrogenated aromatic rings are partly aligned, while in its trans form the dipoles are pointing in opposite directions and thus their fields are largely canceled. In non-polar solvents (toluene), NPs covered by the less polar trans-azobenzene did not assemble, while those covered by the more polar cis-azobenzene assembled. The self-assembled cis-NPs form cavities suitable for reactions of captured polar molecules, schematically shown in Fig. 8 B.

The NP-self-assembly in toluene was MD-simulated using atomistic force fields of trans- and cis-azobenzene ligands, *separately* obtained by standard optimization steps with the MP2-method. Bulk vdW coupling between the NPs was also implemented. The results of 15 ns long simulations, presented in Fig. 8 C, show that only cis-coated NPs self-assembled, in agreement with the experiments. Upon self-assembly, each of the cis-coated NPs captured on average 5 −7 water molecules, which were dissolved to saturation in toluene (red).

In general, NPs covered with aromatic or chemically active ligands can provide novel types of interactions that can be described by *ab initio* methods. Beside, typical vdW or multipolar Coulombic coupling, one can expect interactions based on $\pi-\pi$-stacking, dipole-lone pair coupling or other exotic coupling mechanisms. For example, Fig. 8 D shows the structures of cis/trans-azobenzene coupled with benzene units, optimized by the MP2 method with the 6–31 g* basis set. To properly describe such interactions in MD simulations, we need to calculate the binding energies of various ligand configurations and integrate them in classical forcefields. In principle, we could also improve the classical MD simulations by going go beyond the Newtonian (Langevin) dynamics, where molecular vibrations and rotations are described by classical analogs of quantum "coherent states", and describe them by classical analogs of quantum "thermalized states". This might improve the stability of self-assembled systems, which currently manifest dramatic coherent motions of the molecular components.

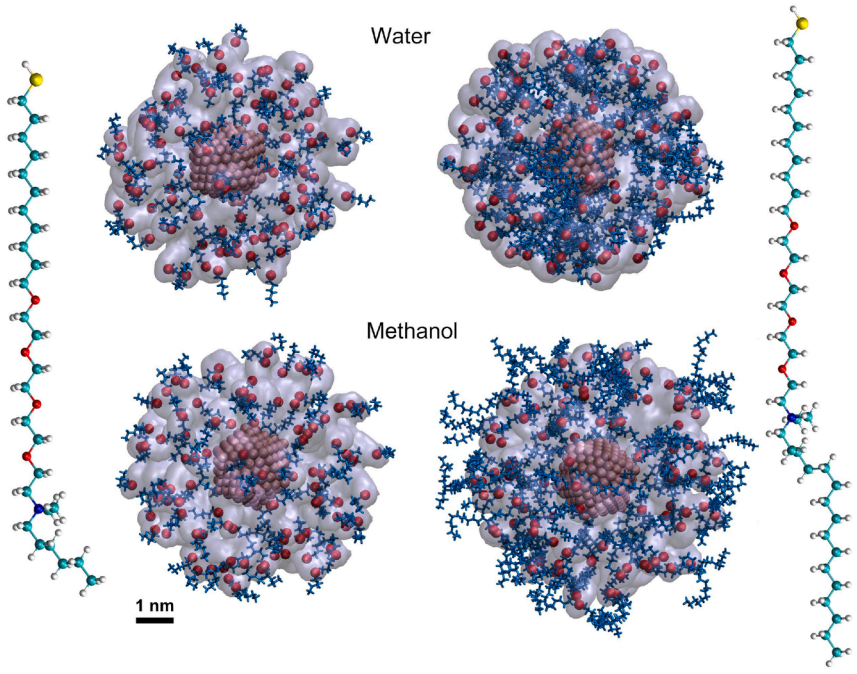

Fig. 7. MD simulations of two NPs differing by the length of terminal alkyl chains in water and methanol solvents. The terminal alkyl chains are shown in blue and the methyl groups at the end of the alkyl chains are shown in red.

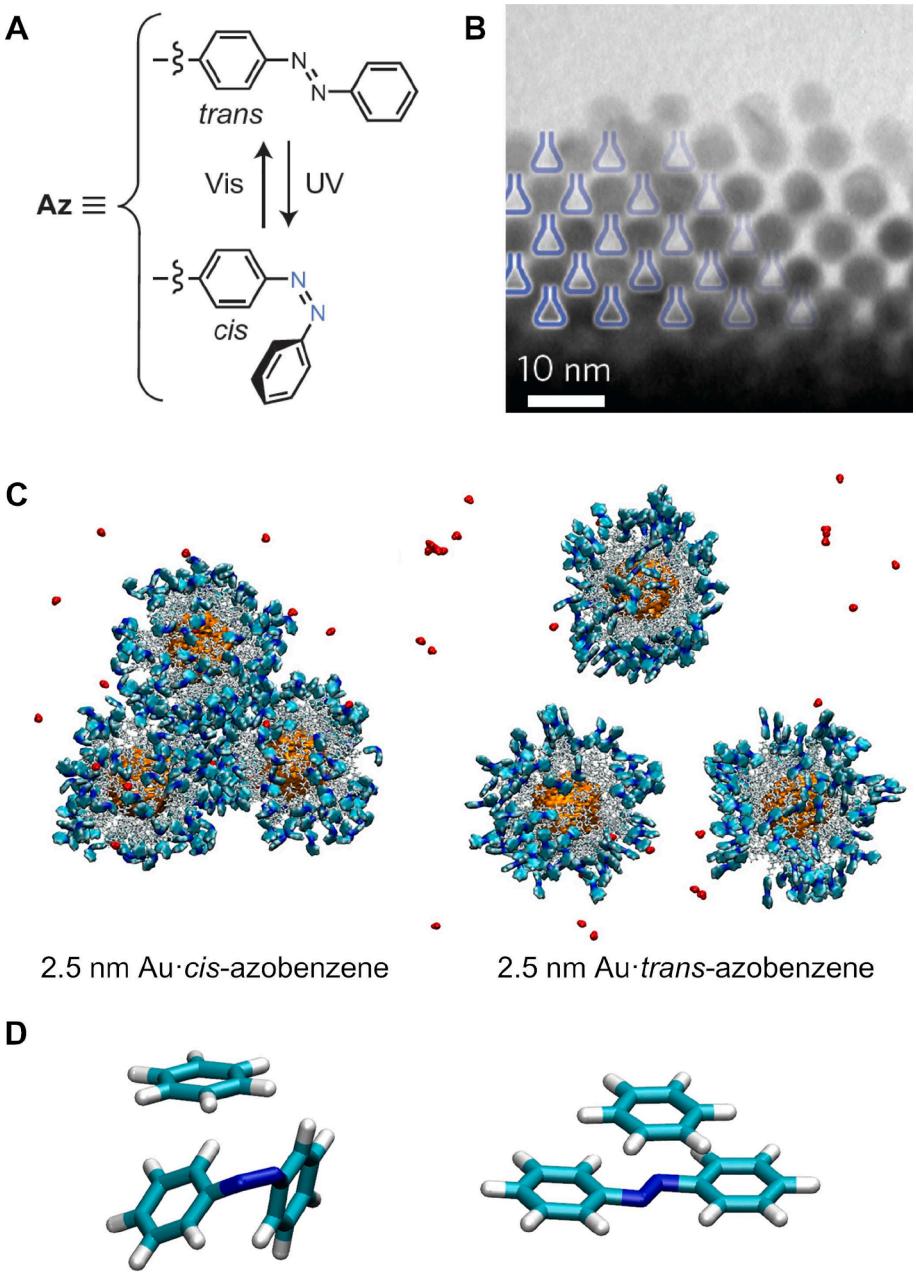

Fig. 8. (A) A light-controlled azobenzene isomerization. (B) Electron micrograph of colloidal crystals prepared by exposing 6 nm Au NPs to ultraviolet light. (C) MD simulations of cis- (left) and trans-azobenzene (right) covered NPs showing different solvation behavior in non-polar toluene. Dissolved water molecules (red) become captured by the cis-NPs. (D) The most stable configurations of molecular heterodimers formed from cis- (left) and trans-azobenzene (right) and benzene calculated by *ab initio* methods.

4.5. Self-assembly of NPs at interfaces of ionic solutions

Nanoparticles can often start to self-assemble when their solvents are gradually removed, which can dramatically increase the NP-NP coupling. Heterogeneous conditions present at solvent surfaces and interfaces can also promote the NPs self-assembly [60]. In an intriguing example of this behavior, supercharged Au NPs (2 nm core) coated with ≈ 100 trimethylammonium TTMA$^+$ ligands were self-assembled at the interface of immiscible electrolytes formed by (5 mM) NaCl in water and bis(triphenyl phosphoranylidene) ammonium tetrakis pentafluorophenyl borate ions BTPPA$^+$ TPFB$^-$ (5 mM) in 1,2-dichloroethane, as shown in Fig. 9 A (NPs not visualized). The electric field controlled the ion concentrations (NP-screening) at the interface of the two immisible ionic solutions. These NPs self-assembled into a close-packed monolayer formed at the interface of both electrolytes, where the NPs were partly

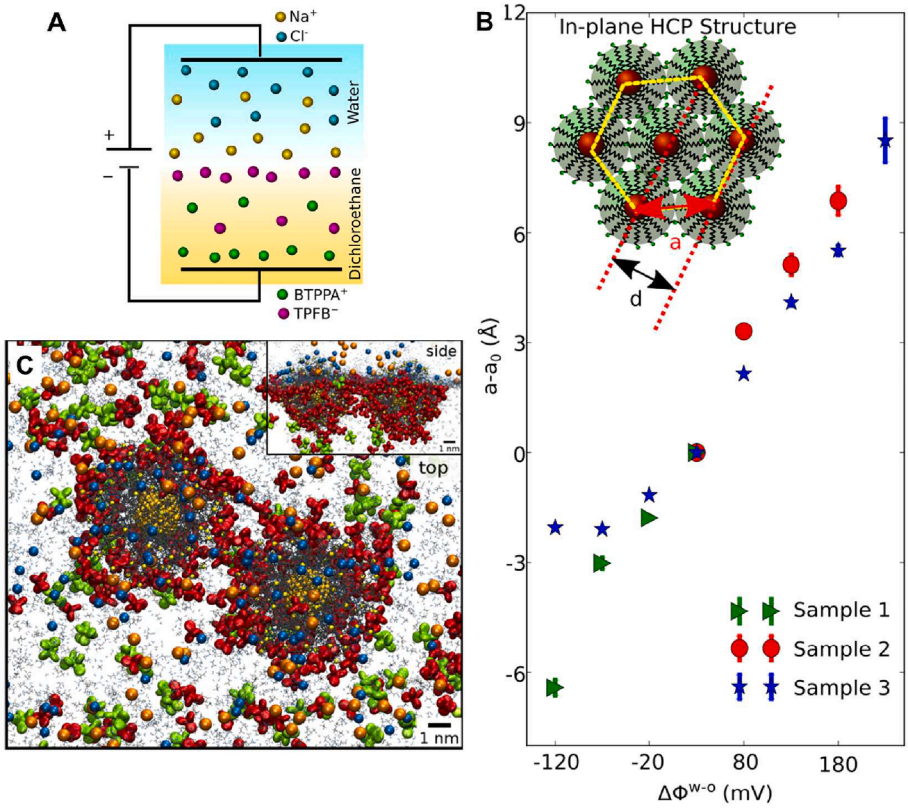

Fig. 9. (A) Cartoon of ion distribution near an interface of two immiscible electrolytes when an electric potential difference is applied between the bulk phases (NPs not shown). (B) Change in the nearest neighbor spacing a for different samples as a function of an electrode potential. (top inset) Cartoon of the 2D hexagonal close-packed structure of NPs with nearest-neighbor spacing a. (C) Two super-charged NPs simulated at the interface of two immiscible electrolytes form a stable pair at $t = 68$ ns (top and side views).

submerged in both electrolytes. Interestingly, the lattice constant a of this monolayer was tunable by an electric field (orthogonal to the monolayer), which was generated by electrodes submerged in the two electrolytes, as shown in Fig. 9 B.

To understand these observations, $1-2$ NPs were atomistically simulated at the interface of the electrified electrolytes positioned in a large box [60]. Initially, organic $TPFB^-$ ions condensed onto the charged NPs, thereby pulling them from the aqueous-side of the interface to the (low permittivity) organic-side, but contiguous to the interface (Fig. 9 C). The NP-submergence was sensitive to the electrode charging, where the fictive electrification was modeled by opposite charging of the two electrolytes (redundant ions accumulated at the interface). When NP-pairs were simulated at the interface of electrolytes, the organic $TPFB^-$ ions formed chains acting as bridging molecules connecting the $TTMA^+$ ligands of different NPs. The structure of these chains and the NP separations could be controlled by the ion concentrations at the interface. This example illustrates the complexity of NP-self-assembly processes at interfaces, requiring a precise atomistic modeling.

4.6. Self-assembly of NPs at liquid–air interfaces

Different NPs positioned at liquid–air interfaces can also form many binary NPs superlattices (BNSLs) [14]. For example, when 5.2 nm dodecanethiol-protected Au NPs and 10.6 nm oleate-protected Fe_3O_4 NPs, solvated at different stoichiometries in evaporating hexane, were positioned at the DEG(non-solvent)-air interface, the NPs were observed to self-assemble into BNSLs with less than 10 layers. These BNSLs can be used to form nanoporous materials by removing one type of NPs (calling the missing NP *vac*) and sintering the remaining NPs. Detailed analysis of AB_4 (i.e., $(\text{-}AB_4\text{-})_n$), AB_5 (i.e., $(\text{-}AB_4\text{-}B_2\text{-}AB_4\text{-})$), AB_6 (i.e., $(\text{-}AB_4\text{-}B_2\text{-})_n$, AB_{11} (i.e., $(\text{-}AB_4\text{-}B_7\text{-})_n$, Figs. 10 A-C), and other lattices has revealed that BNSLs with similar relative sizes of NPs have the same or slightly reorganized AB_4 bottom monolayer in contact with DEG, irrespective of the overall NPs stoichiometry in the formed lattices. This AB_4 structure provides a maximum coverage of the liquid surface. The absence of such "guiding structures" in bulk self-assemblies suggests a profound effect of the air–liquid interface.

Let's first examine this effect by semi-analytical modeling. The NP-NP coupling free energies in solution are much smaller than in air; they are roughly given by the NP-NP coupling free energies in air decreased by the NP-solvent coupling free energies calculated only in the area of the released NP. The relevance of a liquid interface in the formation of certain BNSLs (at the air–liquid interface) can be estimated from the ratio of NP-NP (air) and (floating) NP-liquid coupling free energies. The last energy can be estimated as follows.

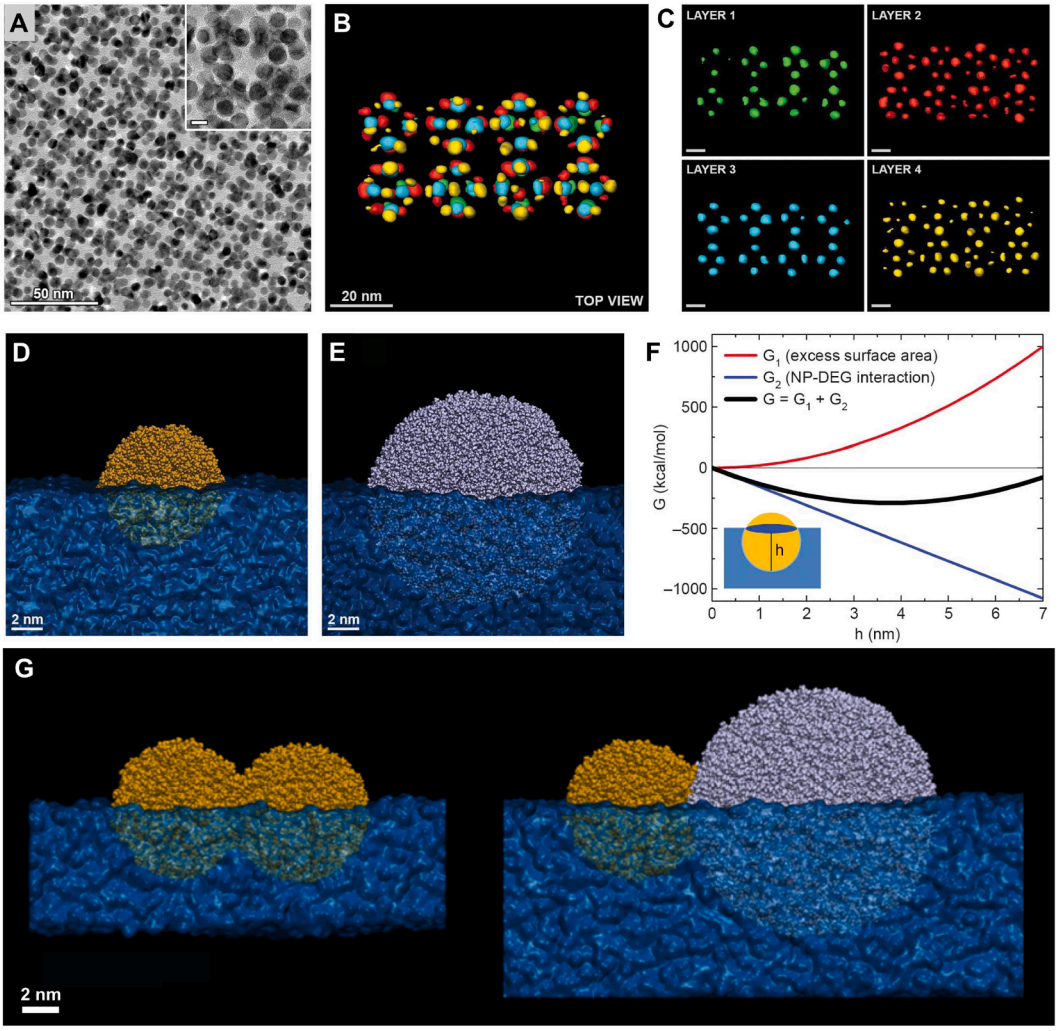

	NPs per unit cell		Contact types and their counts					
BNSL	Au	Fe_3O_4	Au-DEG	Fe_3O_4-DEG	Au-Au	Au-Fe_3O_4	Fe_3O_4-Fe_3O_4	E (kcal/mol)
AB_4	8	2	4	1	9	20	0	17,900
AB_6	12	2	4	1	12	24	0	19,930
AB_{11}	22	2	4	1	50	24	1	29,910

Fig. 10. (A) TEM image of vac_1Au_{11}-type arrays terminated with Au NPs. (B) 3D representation of a part of the reconstructed segmented volume of a vac_1Au_{11}-type array. (C) Four different layers of a vac_1Au_{11}-type array shown separately for clarity. Scale bars is 10 nm. (bottom) (D and E) Atomistic models of (D) a dodecanethiol-functionalized 5-nm Au NP and (E) an oleate-functionalized 10 nm Fe_3O_4 NP relaxed at the DEG-vacuum interface. (F) Free energy as a function of immersion height, *h*, for a 5-nm Au NP (protected with a 1-nm-thick ligand shell) immersed into DEG. Red, energy cost to create excess DEG surface area; blue, favorable binding free energy of DEG and Au NP; black, total energy. (G) Au-Au and Au-Fe_3O_4 NPs pairs at the DEG-vacuum interface. (H) Estimated lattice energies for AB_4, AB_6, and AB_{11} BNSLs.

Immersing NP in a liquid has a Gibbs free energy cost of $G_1 = \gamma A_{excess}$, where A_{excess} is an excess liquid surface area (cavity) formed and γ is a liquid surface tension. G_1 is offset by a NP-liquid coupling free energy of $G_2 = G^\circ A_{immerse}$, where G° is a free energy of a NP-ligands-to-liquid binding per unit area, and $A_{immerse}$ is the immersed surface area of NP. These energies can be illustrated on a model calculation performed for a 5 nm dodecanethiol-decorated Au NP, protected with a 1 nm-thick ligand shell, immersed into DEG, where $G^\circ \approx -7$ kcal/(mol·nm^2) and $\gamma \approx 45$ dyne/cm. Dependences of G_1, G_2, and $\Delta G = G_1 + G_2$ on the NP-immersion height *h*, shown in Fig. 10 F, reveal that this NP is stabilized when it is roughly half-submerged in DEG [14], where $\Delta G \approx -300$ kcal/mol. This large value is comparable to the NP-NP (air) coupling free energy, showing that the NP-liquid coupling is an important factor in the NPs self-

assembly.

Atomistic MD simulations presented in Figs. 10 D, E revealed that both types of NPs (with dodecanethiol and oleate ligands) are also roughly half submerged in DEG, as predicted in Fig. 10 F. Moreover, MD simulations can reveal why certain lattice types are stabilized. They have shown that the small dodecanethiol-covered Au NP and large oleate-protected Fe_3O_4 NP have NP-DEG coupling energies (enthalpies) of 1,200 and 4,450 kcal/mol, respectively, which are similarly proportional to their respective NP-surface areas. In contrast, the NP-EG (ethylene glycol) coupling energies are disproportional to the NP-surface areas, which shows that EG can distinguish between the two ligand types; as a result, these different NPs couldn't share well the EG surface and their self-assembly is problematic [14]. Notice again these NP-liquid coupling energies are large compared to the NP-NP coupling energies between exposed or partly submerged NPs of ≈ 300 kcal/mol, shown in Fig. 10 G. Hence, NPs in the first self-assembled layer exhibit a high affinity to DEG, which they tend to cover in the most efficient way.

These NP-liquid and NP-NP binding energies can be used to approximately evaluate lattice energies of different BNSLs [14]. Fig. 10 H provides lattice energies (per unit cell) for the AB_4, AB_6, and AB_{11} lattices, using the appropriate number of contact points within their unit cells. In all 3 lattices, the same numbers and types of NPs bind directly to DEG. These contributions add to an energy of 9,250 kcal/mol per unit cell of these BNSLs, which is roughly an order of magnitude larger than the interaction energy between two adjacent monolayers of NPs in AB_6. This supports the profound role of NP-DEG interactions in the stabilization of BNSLs, where the upper NP layers have smaller energy contributions.

NPs of different shapes and ligands can further enrich the self-assembly conditions at liquid–air interfaces [61]. Fig. 11 A shows that nanocubes (NCs) with different ligands either do not submerge (non-solvent), submerge in tilted orientations, or fully submerge (potentially fully solvate) in water. This behavior can be understood from Fig. 11 B, displaying $\Delta G = G_1 + G_2$ calculated analytically for NCs in tilted configurations (body diagonal up) as a function of the submersion height h in DEG for model NC-DEG coupling strengths, G°. For illustrative purposes, the analytical models here were developed for NCs on the DEG surface, due to the availability of parameters for DEG from previous studies. In the limits of small and large $|G^\circ|$, NC is either fully exposed ($G^\circ \geqslant -1$ kcal/(mol·nm^2)) or fully submerged ($G^\circ \leqslant -11$ kcal/(mol·nm^2)). However, for intermediate coupling strengths ($-4 \leqslant G^\circ \leqslant -7$ kcal/(mol·nm^2)), minima in ΔG are observed to form for partly (approximately half) immersed NCs, as in spherical NPs. Fig. 11 C also shows how small NCs clusters tend to self-assemble on water surface.

4.7. Self-assembly of superionic NPs into crystallites

Recently, supercharged Au·MUA and Au·TMA NPs of different sizes (11-mercaptoundecanoate (MUA) and (11-mercaptoundecyl)-N,N,N-trimethylammonium (TMA)) were also observed to self-assemble into different BNSLs and crystallites [62]. Initially, electrically neutral aggregates of oppositely charged colloidal Au NPs were formed in water; about 70% of ligands on Au·TMA NPs were positively charged and 100% of ligands on Au·MUA NPs were negatively charged. Then, these aggregates were disassembled in 2 M $(NH_4)_2CO_3$ water solution. Finally, upon a gradual evaporation of NH_4^+ and CO_3^{2-} ions as ammonia and carbon-dioxide gases, respectively, these

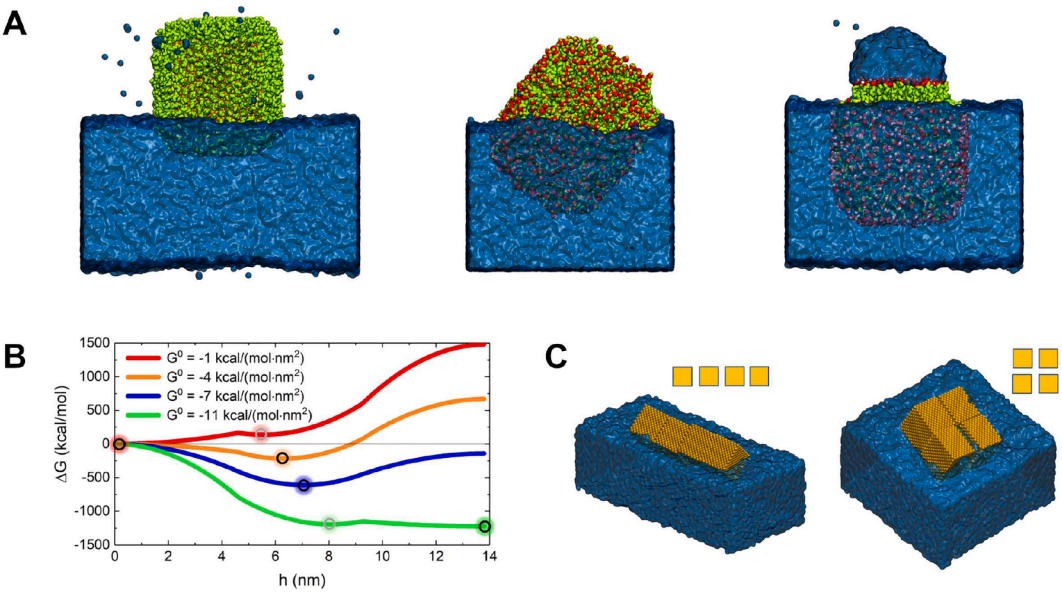

Fig. 11. (A) Three solvation regimes of ligated NCs equilibrated for 100 ns at the water surface. (left to right) NC coated with -S$(CH_2)_{11}CH_3$,-S$(CH_2)_{11}OCH_3$, and -S$(CH_2)_{12}$OH ligands. (B) Total free energy of NC-DEG coupling, ΔG, as a function of NC immersion height, h (body diagonal is vertical). The NC size is as in panel B, but the strengths of favorable interactions between ligands and DEG per unit of contact area are varied according to the values of G° given in the legend. The black and grey circles mark the global and local minima in ΔG, respectively. (C) Self-assembly of four NCs on water for a model strength of vdW coupling to the solvent ($\epsilon = -0.3$ kcal/mol) after $t = 100$ ns of equilibration at $T = 300$ K. [61].

NPs were reassembled into BNSLs, depending on their relative sizes.

With the increasing dissimilarity of NPs sizes, more complex lattice types and crystals were observed to form, such as the AB (CsCl) lattice forming rhombic dodecahedra crystals, the A_3B_4 (Th_3P_4) lattice forming triakis tetrahedra crystals, and other lattices/crystals and amorphous phases. The phase diagram in Fig. 12 A reveals the (experimental and theoretical) coexistence regions of the dominant AB and A_3B_4 lattices, forming the Catalan crystals shown in Fig. 12 B-D. These types of crystals typically form when the components interact with short-range isotropic forces, as in the current systems, which could explain their present formation.

The stabilization of different superionic lattices in strong ionic solutions was studied by atomistic MD simulations and semi-analytical methods. Fig. 12 E shows an example of simulated oppositely charged 5 nm Au NPs immersed in a concentrated (4.3 M) solution of $(NH_4)_2CO_3$. Combining these simulations with umbrella sampling methods, the NP-NP binding free energies as a function of the NP-distances were calculated in Fig. 12 F. At early stages of the NP-self-assembly, when the ionic strength is still large enough, the Coulombic coupling between the NP-superions is highly screened and their stabilization in the formed BNSLs is determined by their local coupling (Yukawa-type potential). We have used these short-range free-energy dependencies to evaluate the free energies of elementary cells in the observed lattices. When these lattice energies were evaluated as a function of the NP-sizes, we obtained the phase diagram in Fig. 12 A, which agrees well with the experiments.

To understand why the given lattices form the observed Catalan crystals, we evaluated the surface free energies of their different facets (separation energies of removed parts of crystals). The facets with absolutely lower surface energies should be less prone to binding new particles and thus more stable. In Fig. 13 A, the surface free energies are calculated for the (100), (110), and (111) facets of the AB lattice. The (110) facet, which has the smallest absolute free energy density, is observed in experiments. In Fig. 13 B, the surface energies are calculated just for the (110) and (211) facets of the A_3B_4 lattice. Here, the (211) facet has much lower absolute free energy

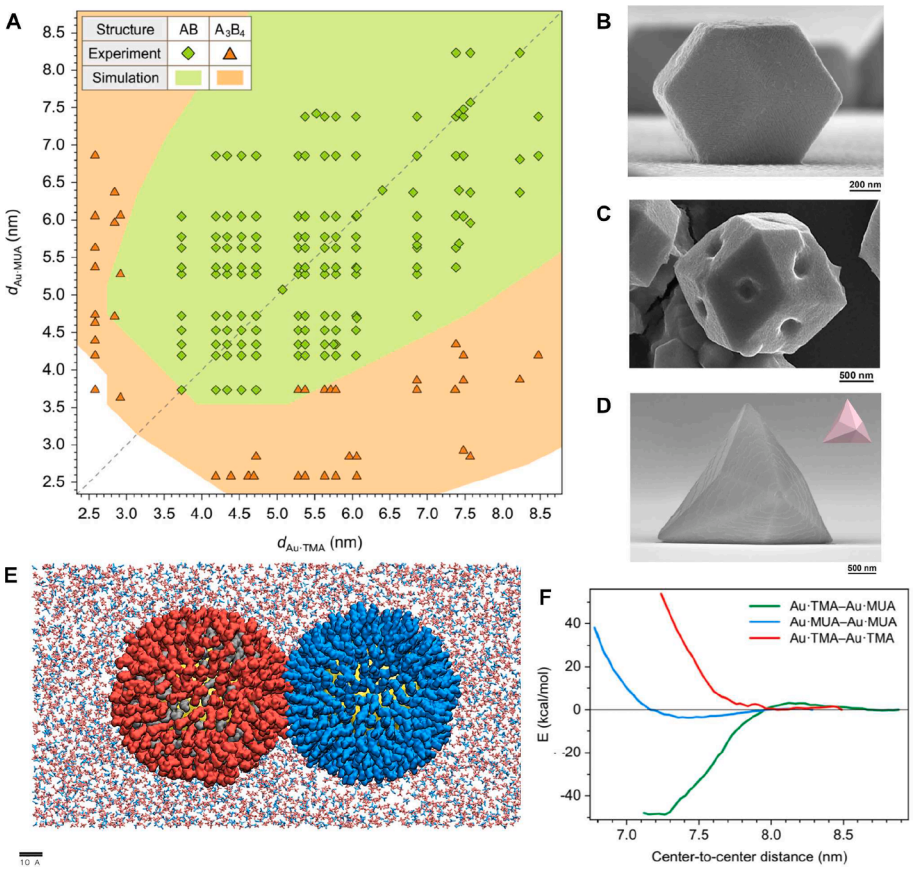

Fig. 12. (A) A phase diagram of the existence regions of different BNSLs obtained in experiments (dotted data) and MD simulations (colored regions), in dependence on the (naked) sizes of ligated NPs (the colored regions correspond to energy minima lower than $--200$ kcal/mol for the CsCl-type lattice and $--150$ kcal/mol for the Th_3P_4-type lattice) (B) The observed rhombic dodecahedra crystal (AB lattice), coassembled from equally sized, 7.42 nm Au·TMA and Au·MUA. (C) The same type of crystal when the NP-charges are likely not balanced due to self-assembly in a weaker ionic solution. (D) A triakis tetrahedra crystal (Th_3P_4-type lattice), coassembled from 5.28 nm Au·TMA and 3.73 nm Au·MUA. (E) Snapshot from an atomistic simulation of two oppositely charged 5 nm Au NPs immersed in a concentrated (4.3 M) solution of $(NH_4)_2CO_3$ (MUA, blue; TMA, red; hexanethiol, gray; Au core, yellow; NH_4^+, red; CO_3^{2--}, blue; water not shown). (F) Free energies of binding between different pairs of 5 nm NPs, calculated by an umbrella sampling technique (each NP is coated with a 1.5 nm-thick monolayer of TMA/MUA, giving rise to an effective diameter of 8 nm; note that TMA is slightly longer than MUA).

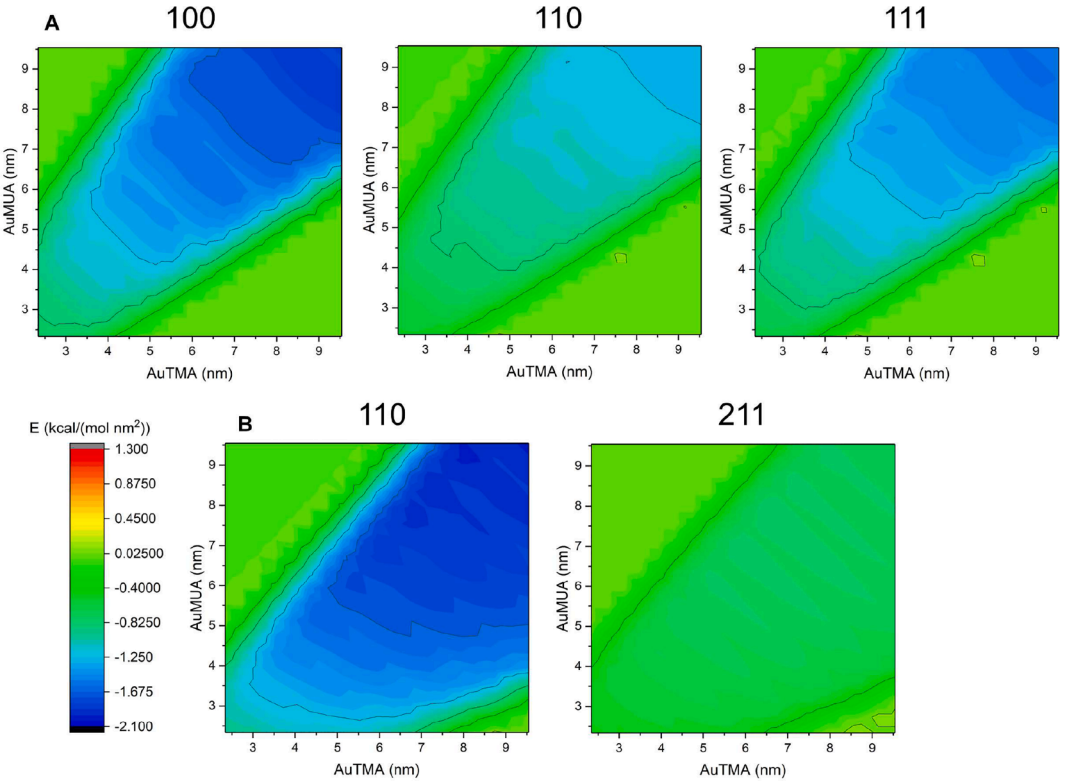

Fig. 13. (top) Surface free energies per nm^2 for: (A) (100), (110), and (111) facets of CsCl (AB) lattice. (B) The same for (110) and (211) facets of Th_3P_4 lattice.

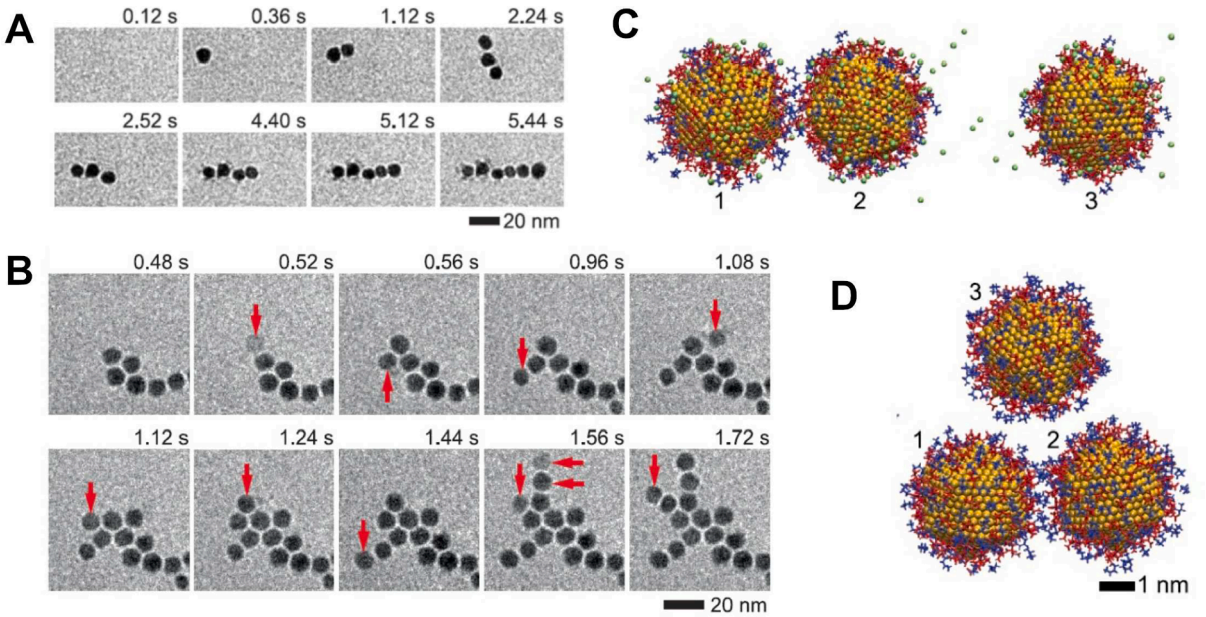

Fig. 14. (A) In situ TEM image sequence showing the growth of Au NPs chains at a (low) concentration of 50 μM of $C_2H_4(NH_3)_2^{2+}$ linkers. (B) The same in the presence of 250 μM of linkers. (C) MD simulations dynamics of NPs when half of the counterions are linkers, and the other half are Na^+ ions. (D) When all the counterions are linkers, NP (3) stays close to linked NP pair (1, 2) and eventually binds to them (branching).

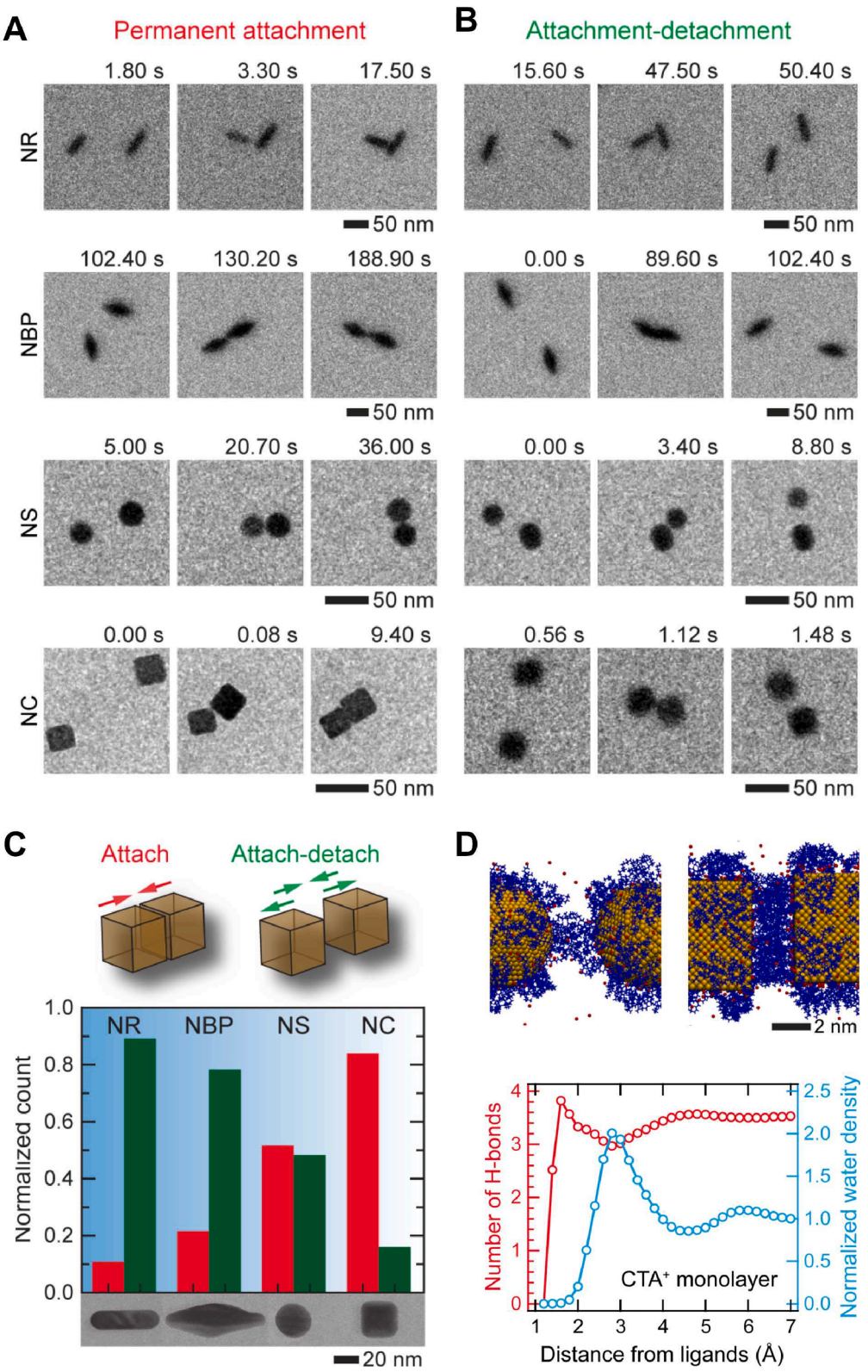

Fig. 15. Interaction dynamics between NPs with different shapes. The pairwise interaction between CTA^{+}-capped NR, NBP, NS, or NC results either in: (A) a permanent attachment or (B) a transient attachment followed by a detachment. (C) The frequency of the permanent attachments (red) and post-attachment detachments (green) between the NPs. The ranking of the likelihood for the permanent attachments following the pairwise contact

is NC > NS > NBP > NR. (D) MD simulations of pairwise attachment of NSs (left) and NCs (right). The overlap of CTA^+ is greater for the attached NCs than for the NSs. (graphs) The number of H-bonds per water (red) molecule and normalized water density (blue) as a function of distance from ligands for a monolayer of CTA^+, capping the surface of gold NPs.

density than the (110) facet, and it is also observed to form. In weaker ionic solutions, the crystals formed with holes (Fig. 12 C) and various protrusions, possibly revealing a poorly screened long-distant Coulombic repulsion between NPs with uncompensated charges, in analogy to nanoshells formed by charged NPs in weaker ionic solutions, as shown in Fig. 6.

5. Atomistic modeling of NPs self-assembling in *in situ* experiments

Lately, NP-self-assembly experiments were conducted in liquid cells by *in situ* TEM with the goal to better understand the self-assembly processes through dynamical observations, such as in the multistep nucleation and growth of NPs [32] and MOFs [63]. In combination with realistic modeling, this hybrid approach can reveal better the nature of NP-self-assembly processes that are otherwise observed only in their final stages.

5.1. Linker-mediated NPs self-assembly

Chains of self-assembled NPs are possibly the simplest superstructures formed when electric and magnetic dipolar interactions are acting between NPs [33,35]. Using *in situ* TEM imaging in liquid cells, linear and branched NP-chains were observed to form in water from citrate-stabilized spherical 10-nm Au NPs in the presence of ethylenediammonium ($C_2H_4(NH_3)_2^{2+}$) linkers. Highly charged NPs can be connected by hydrogen bonds forming between two -NH_3^+ groups of ethylenediammonium and -COO^- groups of each citrate ligand. In these experiments, different scenarios were observed: (1) NPs didn't assemble in the absence of linkers, (2) linear NPs chains were observed to grow at small linker concentrations of $50-250\mu$M, and (3) branched NPs chains were observed to grow at higher linker concentrations, as shown in Fig. 14 (A, B).

Atomistic MD simulations (Figs. 14 (C, D)) revealed that monovalent Na^+ ions have relatively weak Coulombic coupling to the

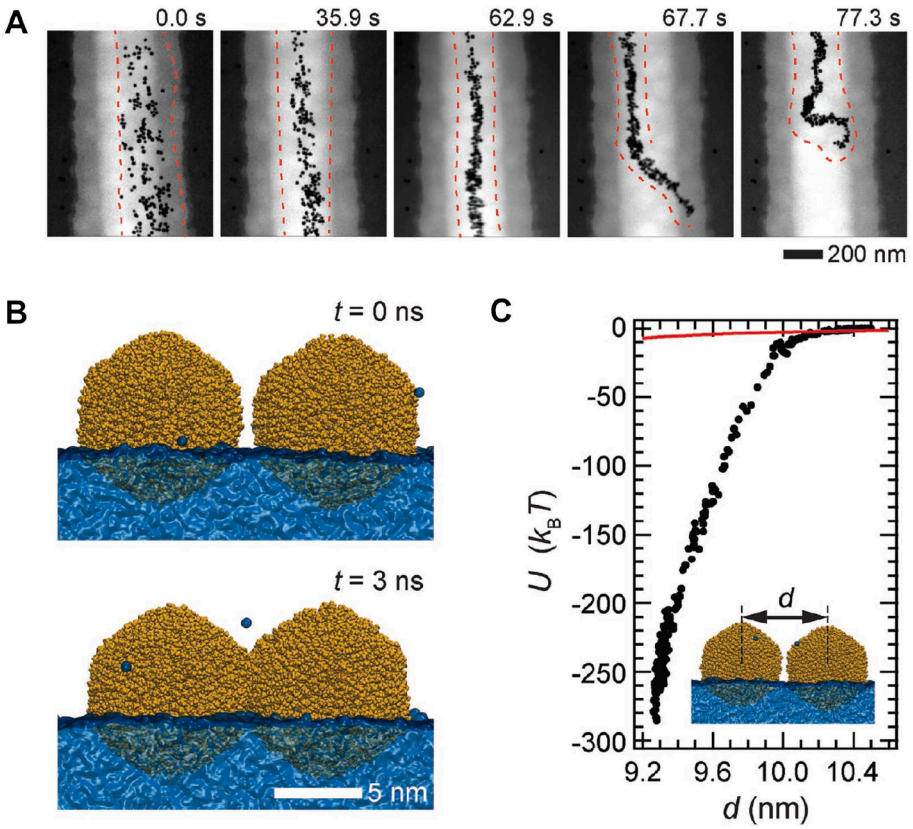

Fig. 16. (A) In situ TEM images of hydrophobic NPs self-assembling on a drying water meniscus present in a nanochannel. (B) (left) MD simulation showing the attachment of the buoyant dodecyl-acrylate-coated 7.8 nm NPs in water through ligand–ligand interactions. (right) The interaction energies between the two Au NPs. The strength of net interaction accounting for both the vdW coupling between the gold cores (alone - red curve) and ligand–ligand coupling are plotted by solid black circles.

highly charged NPs, so they can adsorb on them only partly, while double-charged linkers can adsorb on these NPs via a strong (divalent) Coulombic coupling, but they can't fully neutralize them when the linker concentration in the solution is small. Then these NP-ions complexes remain partly charged, repel each other, and self-assemble at most in linear chains, where they have only a small repulsion. As shown in Fig. 14 (C), individual NPs join the chain in rare events, due to a Coulombic barrier, reduced by a bulk vdW coupling. Once two NPs randomly approach each other, selected linkers can transiently connect them by H-bonds. When the linkers are plentiful, they can practically neutralize these NPs by adsorbing on them and the almost-neutral NP-linkers complexes can self-assemble from any directions (branching), as seen in Fig. 14 (D).

5.2. Self-assembly of hydrophobic NPs of different shapes

It is of interest to investigate how the NP-coupling depends on geometrical parameters, such as NP-volumes, surfaces, and shapes [64]. Recent *in situ* TEM experiments revealed a competition of size/shape-dependent interactions during the self-assembly of NPs capped with a monolayer/bilayer of amphiphilic cetyltrimethylammonium bromide (CTAB) surfactants in water [65]. Fig. 15 (A,B) shows that NPs of different shapes and sizes, such as nanorods (NR), nanobipyramids (NBP), nanospheres (NS), and nanocubes, can all become attached and detached during their coupling (Fig. 15 (C)), but the likelihood of their permanent attachment (red) and post-attachment detachment (green) can be very different. For example, NCs were detached only in rare events, when they had weak edge-to-edge or edge-to-face attachments.

To better understand these *in situ* observations, atomistic MD simulations were performed to model different NPs capped with CTA^+ (ionized CTAB) monolayers/bilayers and Br^- counterions, as shown in Fig. 15 (D). The simulations have revealed a hydrophobic attraction between CTA^+-covered NPs, i.e. their limited solubility in water. In the first water layer, located 2.8 Å away from the CTA^+ ligands, the water (oxygen) density is higher than in bulk, but water molecules in this layer have on average ≈ 3 H-bonds, which is $\approx 15\%$ less than ≈ 3.5 H-bonds for bulk water, revealing the hydrophobic nature of CTA^+. These NPs are also repelled by electrostatic coupling of charged CTA^+, but attracted by a bulk vdW coupling. While the attractive hydrophobic and repulsive Coulombic interactions between NPs are related to their surface areas, the attractive bulk vdW coupling is related to their volumes. Therefore, a preferential face-to-face attachment of NCs reflects their dominant hydrophobic attraction; hydrophobic forces acting between NCs are greater than those between NSs, NBPs, and NRs of similar sizes. In NPs without significant facets, the attractive bulk vdW forces prevail over attractive hydrophobic forces, but they provide a relatively poor competition with the repulsive Coulombic forces [65].

5.3. Templated assembly of NP-filaments within nanochannels

When the solvent evaporates and the non-solvent supports self-assembling NPs, the NP coupling may become highly increased [13,14]. This was also explicitely shown in *in situ* experiments using TEM [66]. Au NPs coated with a hydrophobic alkyl acrylate were floating on water in nanochannels within a liquid cell. When the water non-solvent gradually evaporated, capillary forces brought NPs together, so that NP-chains were formed, as shown in Fig. 16 (A). Atomistic MD simulations revealed that NPs floating on water had $\approx 1/3$ of their height submerged. However, the simulated NPs did not assemble until ≈ 1 nm cut-off, typically present in the force field for a vdW coupling, was extended to 2 nm, so that ligands on different NPs started to attract (Fig. 16 (B)). Then, a strong attachment between neighboring NPs was fast formed with binding energies of $200-300$ kT. This can explain a large elasticity of NPs filaments formed, which folds into itself upon breaking (Fig. 16 (A)).

6. Conclusion

In this Review, we discussed modeling of NPs with complex coupling that can self-assemble into various superstructures. Competing interactions acting between NPs and cooperative phenomena occurring during their self-assembly can be captured at different levels of precision using mean-field, coarse-grained, classical atomistic, and quantum simulation methods. When NPs are coupled via long-range interactions, large systems of many NPs are typically modeled using mean-field methods. On the other hand, when the NP-interactions are more local, but not particularly complex, the self-assembly of many NPs can be studied by coarse-grained methods. As the NP-interactions become more complex, often due to intriguing molecular ligands or solvents, a precise atomistic modeling of small ensembles of NPs should be performed to acquire detailed understanding of forces acting between NPs and to understand the NP-self-assembly mechanisms, which often produce non-trivial superstructures. The presented problems and methods cover a significant spectrum of realistic examples of hybrid computational and experimental studies of self-assembled nanoscale components.

Declaration of Competing Interest

The authors declare that they have no known competing financial interests or personal relationships that could have appeared to influence the work reported in this paper.

Data availability

Data will be made available on request.

Acknowledgments

We would like to thank Rafal Klajn, Nicholas Kotov, and Utkur Mirsaidov for helpful discussions.

References

[1] Nicolis G, Prigogine I. Self-organization in nonequilibrium systems. New York: Wiley; 1977.
[2] Whitesides GM, Mathias JP, Seto CT. Molecular self-assembly and nanochemistry: a chemical strategy for the synthesis of nanostructures. Science 1991;254:1312.
[3] Whitesides GM, Grzybowski B. Self-assembly at all scales. Science 2002;295:2418.
[4] Grzybowski BA, Wilmer CE, Kim J, Browne KP, Bishop KJM. Self-assembly: from crystals to cells. Soft Matter 2009;5:1110.
[5] Murray CB, Kagan CR, Bawendi MG. Self-Organization of CdSe Nanocrystallites into Three-Dimensional Quantum Dot Superlattices. Science 1995;270:1335.
[6] Mann S. Self-assembly and transformation of hybrid nano-objects and nanostructures under equilibrium and non-equilibrium conditions. Nat Mater 2009;8:781.
[7] Henzie J, Grünwald M, Widmer-Cooper A, Geissler PL, Yang P. Self-assembly of uniform polyhedral silver nanocrystals into densest packings and exotic superlattices. Nat Mater 2012;11:131.
[8] Xu L, Ma W, Wang L, Xu C, Kuang H, Kotov NA. Nanoparticle assemblies: dimensional transformation of nanomaterials and scalability. Chem Soc Rev 2013;42:3114.
[9] Jones MR, Seeman NC, Mirkin CA. Programmable materials and the nature of the DNA bond. Science 2015;347:1260901.
[10] Shevchenko EV, Talapin DV, Kotov NA, O'Brien S, Murray CB. Structural diversity in binary nanoparticle superlattices. Nature 2006;439:55.
[11] Nakagawa Y, Kageyama H, Oaki Y, Imai H. Direction control of oriented self-assembly for 1D, 2D, and 3D microarrays of anisotropic rectangular nanoblocks. J Am Chem Soc 2014;136:3716.
[12] Bigioni TP, Lin X-M, Nguyen TT, Corwin EI, Witten TA, Jaeger HM. Kinetically driven self assembly of highly ordered nanoparticle monolayers. Nat Mater 2006;5:265.
[13] Singh G, Chan H, Baskin A, Gelman E, Repnin N, Král P, Klajn R. Self-assembly of magnetite nanocubes into helical superstructures. Science 2014;345:1149.
[14] Udayabhaskararao T, Altantzis T, Houben L, Coronado-Puchau M, Langer J, Popovitz-Biro R, Liz-Marzán LM, Vuković L, Král P, Bals S, Klajn R. Tunable porous nanoallotropes prepared by post-assembly etching of binary nanoparticle superlattices. Science 2017;358:514.
[15] Shevchenko EV, Talapin DV, O'Brien S, Murray CB. Polymorphism in AB13 nanoparticle superlattices: an example of semiconductor-metal metamaterials. J Am Chem Soc 2005;127:8741.
[16] Bishop KJM, Wilmer CE, Soh S, Grzybowski BA. Nanoscale forces and their uses in self-assembly. Small 2009;5:1600.
[17] Lalatonne Y, Richardi J, Pileni MP. Van der Waals versus dipolar forces controlling mesoscopic organizations of magnetic nanocrystals. Nat Mater 2004;3:121.
[18] Yang M, Chan H, Zhao G, Bahng J, Zhang P, Král P, Kotov NA. Self-assembly of nanoparticles into biomimetic capsid-like nanoshells. Nat Chem 2016;9:287.
[19] Sanchez-Iglesias A, Grzelczak M, Altantzis T, Goris B, Perez-Juste J, Bals S, Van Tendeloo G, Donaldson S, Chmelka B, Israelachvili J, Liz-Marzan L. Hydrophobic interactions modulate self-assembly of nanoparticles. ACS Nano 2012;6:11059.
[20] Lin G, Chee SW, Raj S, Král P, Mirsaidov U. Linker-mediated self-assembly dynamics of charged nanoparticles. ACS Nano 2016;10:7443.
[21] Tang Z, Zhang Z, Wang Y, Glotzer SC, Kotov NA. Self-assembly of CdTe nanocrystals into free-floating sheets. Science 2006;314:274.
[22] K. Miszta, J. de Graaf, G. Bertoni, D. Dorfs, R. Brescia, S. Marras, L. Ceseracciu, R. Cingolani, R. van Roij, Rene and M. Dijkstra, Hierarchical self-assembly of suspended branched colloidal nanocrystals into superlattice structures, Nat. Mater. 10, 872 (2011).
[23] Wang T, Zhuang J, Lynch J, Chen O, Wang Z, Wang X, LaMontagne D, Wu H, Wang Z, Cao YC. Self-assembled colloidal superparticles from nanorods. Science 2012;338:368.
[24] Yeom J, Yeom B, Chan H, Smith K, Dominguez-Medina S, Bahng J, Zhao G, Chang W, Chang S, Chuvilin A, Melnikau D, Rogach A, Zhang P, Link S, Král P, Kotov NA. Chiral templating of Self-assembling nanostructures by cicircular polarized light. Nat Mater 2014;14:66.
[25] Bouju X, Duguet E, Gauffre F, Henry CR, Kahn ML, Mélinon P, Ravaine S. Nonisotropic self-assembly of nanoparticles: from compact packing to functional aggregates. Adv Mater 2018;30:1706558.
[26] Glotzer SC, Solomon MJ. Anisotropy of building blocks and their assembly into complex structures. Nat Mater 2007;6:557.
[27] Zhu G, Huang Z, Xu Z, Yan L-T. Tailoring interfacial nanoparticle organization through entropy. Acc Chem Res 2018;51:900.
[28] Grzelak D, Szustakiewicz P, Tollan C, Raj S, Král P, Lewandowski W, Liz-Marzán LM. In situ tracking of colloidally stable and ordered assemblies of gold nanorods. J Am Chem Soc 2020;142:18814.
[29] Li T, Sknepnek R, Macfarlane R, Mirkin C, Olvera de la Cruz M. Modeling the crystallization of spherical nucleic acid nanoparticle conjugates with molecular dynamics simulations. Nano Lett 2012;12:2509.
[30] Schapotschnikow P, Pool R, Vlugt TJH. Molecular simulations of interacting nanocrystals. Nano Lett 2008;8:2930.
[31] Choueiri RM, Klinkova A, Thérien-Aubin H, Rubinstein M, Kumacheva E. Structural transitions in nanoparticle assemblies governed by competing nanoscale forces. J Am Chem Soc 2013;28:10262.
[32] Loh N, Sen S, Bosman M, Tan S, Zhong J, Nijhuis C, Král P, Matsudaira P, Mirsaidov U. Multistep nucleation of nanocrystals in aqueous solution. Nat Chem 2016;9:77.
[33] Talapin DV, Shevchenko EV, Murray CB, Titov AV, Král P. Dipole-dipole interactions in nanoparticle superlattices. Nano Lett 2007;7:1213.
[34] Titov AV, Král P. Modeling the self-assembly of colloidal nanorod superlattices. Nano Lett 2008;8:3605.
[35] Baskin A, Lo W-Y, Král P. Clusters and lattices of particles stabilized by dipolar coupling. ACS Nano 2012;6:6083.
[36] Hamaker HC. The London—van der Waals attraction between spherical particles. Physica 1937;4:1058.
[37] Singh G, Chan H, Udayabhaskararao T, Gelman E, Peddis D, Baskin A, Leitus G, Král P, Klajn R. Magnetic field-induced self-assembly of iron oxide nanocubes. Faraday Discuss 2015;181:403.
[38] Chan H, Král P. Self-standing nanoparticle membranes and capsules. Nanoscale 2011;3:1881.
[39] Titov AV, Král P, Pearson R. Sandwiched graphene-membrane superstructures. ACS Nano 2010;4:229.
[40] Patra N, Wang B, Král P. Nanodroplet Activated and Guided Folding of Graphene Nanostructures. Nano Lett 2009;9:3766.
[41] Patra N, Song Y, Král P. Self-assembly of graphene nanostructures on nanotubes. ACS Nano 2011;5:1798.
[42] Chan H, Král P. Sandwiched nanoparticle-lipid superstructures. ACS Omega 2018;3:10631.
[43] Pogodin S, Werner M, Sommer J-U, Baulin VA. Nanoparticle-induced permeability of lipid membranes. ACS Nano 2012;6:10555.
[44] Van Lehn RC, Ricci M, Silva PHJ, Andreozzi P, Reguera J, Voitchovsky K, Stellacci F, Alexander-Katz A. Lipid tail protrusions mediate the insertion of nanoparticles into model cell membranes. Nat Commun 2014;5:4482.
[45] Su C-F, Merlitz H, Rabbe H, Sommer J-U. Nanoparticles of various degrees of hydrophobicity interacting with lipid membranes. J Phys Chem Lett 2017;8:4069.
[46] Sen S, Han Y, Rehak P, Vuković L, Král P. Computational studies of micellar and nanoparticle nanomedicines. Chem Soc Rev 2018;47:3849.
[47] Humphrey W, Dalke A, Schulten K. VMD: Visual molecular dynamics. J Mol Graph 1996;14:33.
[48] Vanommeslaeghe K, Hatcher E, Acharya C, Kundu S, Zhong S, Shim J, Darian E, Guvench O, Lopes P, Vorobyov I, Mackerell Jr AD. CHARMM general force field: A force field for drug-like molecules compatible with the CHARMM all-atom additive biological force fields. J Comput Chem 2010;31:671.
[49] Phillips J, Braun R, Wang W, Gumbart J, Tajkhorshid E, Villa E, Chipot C, Skeel R, Kale L, Schulten K. Scalable molecular dynamics with NAMD. J Comput Chem 2005;26:1781.
[50] Darden T, York D, Pedersen L. Particle Mesh Ewald: An N.log(N) Method for Ewald Sums in Large Systems. J Chem Phys 1993;98:10089.
[51] He J, Lin X-M, Chan H, Vuković L, Král P, Jaeger HM. Diffusion and filtration properties of self-assembled gold nanocrystal membranes. Nano Lett 2011;11:2430.

[52] Chan H, Demortiere A, Vuković L, Král P, Petit C. Colloidal nanocube supercrystals stabilized by multipolar coulombic coupling. ACS Nano 2012;6:4203.
[53] Xia Y, Nguyen TD, Yang M, Lee B, Santos A, Podsiadlo P, Tang Z, Glotzer SC, Kotov NA. Self-assembly of self-limiting monodisperse supraparticles from polydisperse nanoparticles. Nat Nanotechnol 2011;6:580.
[54] Sawczyk M, Klajn R. Out-of-equilibrium aggregates and coatings during seeded growth of metallic nanoparticles. J Am Chem Soc 2017;139:17973.
[55] Kadupitiya JCS, Fox GC, Jadhao V. Machine learning for parameter auto-tuning in molecular dynamics simulations: Efficient dynamics of ions near polarizable nanoparticles. Int J High Perf Comp App 2020;34:357.
[56] Li TING, Sknepnek R, de la Cruz MO. Thermally active hybridization drives the crystallization of DNA-functionalized nanoparticles. J Am Chem Soc 2013;135:8535.
[57] Chu Z, Han Y, Bian T, De S, Král P, Klajn R. Supramolecular control of azobenzene switching on nanoparticles. J Am Chem Soc 2018;141:1949.
[58] Monego D, Kister T, Kirkwood N, Mulvaney P, Widmer-Cooper A, Kraus T. Colloidal stability of apolar nanoparticles: role of ligand length. Langmuir 2018;34:12982.
[59] Zhao H, Sen S, Udayabhaskararao T, Sawczyk M, Kučanda K, Manna D, Kundu P, Lee J, Král P, Klajn R. Reversible occlusion and reaction acceleration within dynamically self-assembling nanoflasks. Nat Nanotechnol 2016;11:82.
[60] Bera MK, Chan H, Moyano DF, Yu H, Tatur S, Amoanu D, Bu W, Rotello VM, Meron M, Král P, Lin B, Schlossman ML. Interfacial localization and voltage-tunable arrays of charged nanoparticles. Nano Lett 2014;14:6816.
[61] Nitka TA, Král P, Vuković L. Configurations of floating and self-assembling nanoparticles on liquid surfaces. J Phys Chem Lett bf 2019;10:3592.
[62] T. Bian, I. Lobato, T. Altantzis, J. Wang, T.A. Nitka, T.S. Peled, B. Lee, S. Van Aert, L. Vukovic, S. Bals, P. Král, and R. Klajn, Catalan solids from superionic nanoparticles, 10.26434/chemrxiv-2022-klncg, ChemRxiv. Cambridge: Cambridge Open Engage (2022).
[63] Liu X, Chee SW, Raj S, Sawczyk M, Král P, Mirsaidov U. Three-step nucleation of metal-organic framework nanocrystals. PNAS 2021;128. e2008880118.
[64] Grzelak D, Szustakiewicz P, Tollan C, Raj S, Král P, Lewandowski W, Liz-Marzán LM. In situ tracking of colloidally stable and ordered assemblies of gold nanorods. J Am Chem Soc 2020;142:18814.
[65] Tan SF, Raj S, Bisht G, Annadata HV, Nijhuis CA, Král P, Mirsaidov U. Nanoparticle interactions guided by shape-dependent hydrophobic forces. Adv Mater 2018;30:1707077.
[66] Miele E, Raj S, Baraissov Z, Král P, Mirsaidov U. Dynamics of templated assembly of nanoparticle filaments within nanochannels. Adv Mater 2017;29:1702682.